nature structural & molecular biology

Article

https://doi.org/10.1038/s41594-024-01464-7

Structure and catalytic mechanism of exogenous fatty acid recycling by AasS, a versatile acyl-ACP synthetase

Received: 4 October 2023

Accepted: 29 November 2024

Published online: 10 January 2025

Check for updates

Haomin Huang[1,8], Chen Wang[2,8], Shenghai Chang[2,8], Tao Cui[3,8], Yongchang Xu[1], Man Huang[1], Huimin Zhang[4], Chun Zhou[5] ✉, Xing Zhang[2,6] ✉ & Youjun Feng[1,7] ✉

Fatty acids (FAs) are essential building blocks for all the domains of life, of which bacterial de novo synthesis, called type II FA synthesis (FAS II), is energetically expensive. The recycling of exogenous FAs (eFAs) partially relieves the FAS II demand and, therefore, compromises the efficacy of FAS II-directed antimicrobials. The versatile acyl-acyl carrier protein (ACP) synthetase, AasS, enables bacterial channeling of diverse eFA nutrients through holo-ACP, an activated form of ACP. However, the molecular mechanism for AasS catalysis is not fully understood. Here we report a series of cryo-electron microscopy structures of AasS from the bioluminescent bacterium *Vibrio harveyi* to provide insights into the catalytic cycle. AasS forms a ring-shaped hexamer, with each protomer folding into two distinct domains. Biochemical and structural analysis suggests that AasS accommodates distinct eFA substrates and the conserved W230 residue has a gating role. Adenosine triphosphate and Mg^{2+} binding converts the AasS hexamer to a tetramer, which is likely needed for the acyl adenylate intermediate formation. Afterward, AasS reverts to the hexamer conformation in adaption to acyl-ACP production. The complete landscape for eFA scavenging lays a foundation for exploiting the versatility of AasS in biopharmaceuticals.

Fatty acids (FAs) are vital elements required by all the domains of life, in that they contribute to cell membrane formation and provide precursors for vitamin synthesis[1]. In general, the pathways of FA synthesis (FAS) are carried out through two routes, facilitated by enzymes with varying architectures: (1) mammalian and fungal type I FAS (FAS I) and (2) plant plastid and bacterial type II FAS (FAS II)[1,2]. Unlike the FAS I system that is a single large, multifunctional polypeptide, the bacterial FAS II path relies on a series of discrete monofunctional enzymes[2]. The iterative FAS II cycle consists of four steps (condensation, reduction, dehydration and reduction), which lead to the elongation of FAs with two carbon units each round[1,2]. The arsenal of FAS II enzymes is essential for bacterial viability, suggesting the potential of FAS II-directed antibiotic discovery[3–5]. Central to the FAS II pathway, the acyl carrier protein (ACP) shuttles the growing fatty acyl cargos sequestered by diverse ACP-dependent enzymes through the interior hydrophobic sleeves[6]. These enzymes include but are not limited to (1) yeast FA synthase[7]; (2) bacterial 3-hydroxyacyl-ACP dehydratase FabA[8] and FabZ[9] plus FabX, a bifunctional dehydrogenase–isomerase enzyme[10,11]; and (3) certain enzymes of two fatty acyl cofactors lipoic acid and biotin (that is, the LipB octanoyltransferase of lipoic acid synthesis[12] and two biotin synthetic enzymes P450 (BioI)[13] plus the BioH pimeloyl-ACP demethylase[14]). The universal mechanism called 'chain flipping' enables the partition of 4′-phosphopantetheine (Ppan)-tethered fatty acyl chains from the hydrophobic ACP bundle into the other hydrophobic

A full list of affiliations appears at the end of the paper. ✉e-mail: chunzhou@zju.edu.cn; xzhang1999@zju.edu.cn; fengyj@zju.edu.cn

groove in the vicinity of the enzymatic catalysis center[15]. Blocking the FAS II pathway resensitizes mobile colistin resistance (*mcr-1*)-harboring *Enterobacter* to colistin, a 'last-resort' antibiotic[16]. Diverse bacterial species are capable of assimilating extracellular FA (eFA) from environments to build their membrane phospholipids and gain growth advantages by circumventing the need to make FAs for lipid synthesis[3,17]. This poses the question of whether bacterial pathogens hijack host FAs to bypass metabolic essentiality of their FAS II pathways[18], which in turn compromises the efficacy of FAS II-targeted inhibitors[5,19].

So far, three eFA recycling mechanisms have been determined[3,17,20]. The first is the conversion of FA to acyl-CoA thioesters by *Escherichia coli* FadD, the paradigm acyl-CoA synthetase[3,21]. The second is the production of acyl-ACP species by an acyl-ACP synthetase (AasS) that was initially detected in *E. coli*[22–24] and the bioluminescent bacterium *Vibrio harveyi*[25–27]. The third is the formation of acyl-phosphates (acyl-P) by an FA kinase (Fak) system composed of two dissociable subunits[28,29] (that is, FakA kinase[30,31] and FakB, an FA-carrying partner[31–34]). In *E. coli* and its relatives, in addition to entry into the tricarboxylic acid cycle to produce adenosine triphosphate (ATP) molecules[3], long-chain acyl-CoA begins phosphatidic acid synthesis through PlsB (glycerol-3-phosphate (G3P) acyltransferase) connected with PlsC (lysophosphatidic acid acyltransferase)[35–37]. In Gram-negative bacteria carrying the system of AasS combined with PlsX (phosphate:acyl-ACP acyltransferase) and PlsY (acyl-P dependent G3P acyltransferase), acyl-ACP thioester is an initiator for phosphatidic acid synthesis[1,38]. In contrast, Gram-positive microbes that harbor Fak and PlsX or PlsY machinery recruit acyl-P as a switcher[28,39]. The discovery of FakA coupled with distinct FakB isoforms (B1 to B5) extends our understanding of bacterial machineries for diverse eFA salvage[28,30–33]. The Fak system remodels the membrane phospholipids of *Staphylococcus aureus*[40,41], which facilitates bacterial infections[42,43] and promotes formation of antibiotic resistance[44]. Thus, it is plausible to design narrow-spectrum, pathogen-specific antibacterial agents targeting eFA salvage and its subsequent use.

The AasS protein belongs to the superfamily of adenylate-forming enzymes and acyl-activating enzymes (AAEs). This AAE family is grouped into three major classes (I–III)[45]. Class I consists of (1) firefly luciferase and oxidoreductase[46–48]; (2) acyl-CoA and aryl-CoA synthetase (formerly fatty acyl-CoA ligase, FACL)[49–51]; (3) AasS (also called fatty acyl-adenosine monophosphate (AMP) ligase, FAAL)[22,27,52]; and (4) nonribosomal peptide synthetase (NRPS) adenylation domains[53–55]. Class II is restricted to a panel of aminoacyl-transfer RNA synthetases[56–59]. Class III is composed of several NRPS-independent siderophore synthetases[45,60]. In general, AAE catalysis proceeds in a 'two-step' reaction: a common first step of adenylation[46,51] and a diverse second step of adenylate transfer[61,62]. During catalysis, the AAE group of enzymes undergoes substantial domain alternation and rearrangement, characterized by an open adenylate-forming conformation and a closed thioester-producing conformation[46,55]. It is challenging to distinguish AasS and FAAL from FACL solely by sequence analyses[63–65]. This is evidenced by the situation that a previously proposed signature motif for FAAL (that is, an insert of ~20 aa) is a controversial indicator for differentiating FAAL activities within 34 mycobacterial FadD homologs[63–66]. Therefore, the exact assignment of AasS and FAAL activities requires biochemical assays coupled with in silico search.

In the past 30 years since its discovery[25–27], the AasS of *V. harveyi* has been genetically and enzymatically described[52,62,67]. It has been shown that AasS is able to activate a variety of FAs with ATP, forming fatty acyl-AMP (the first step of catalysis). The fatty acyl moiety is presumably transferred to the 4′-Ppan group of holo-ACP in the second step of catalysis[52,62]. However, the architecture and detailed catalysis mechanism for AasS remain largely elusive. Here, we report a series of cryo-electron microscopy (cryo-EM) structures composed of one apo form and eight structures of AasS in complex with its cofactors, substrates, intermediates and/or final products. Our findings constitute mechanistic landscapes for eFA recycling by AasS.

Results

AasS forms a hexamer

Unlike the analog FadD, an acyl-CoA ligase (Supplementary Fig. 1), AasS of *V. harveyi* is a functional FAAL member that attaches a variety of FAs to ACP, giving acyl-ACP thioesters (Supplementary Figs. 1–3)[52]. In particular, the promiscuity of substrate selection enables AasS to be regarded as a potential tool enzyme of versatility[62]. Despite prior knowledge of AasS enzymology, its assembly, structure and molecular mechanism of action are poorly understood. *Thermus thermophilus* fatty acyl-CoA synthetase–ligase (ttFACS) is an archetype FACL[49]. In contrast, FadD10 of *M. tuberculosis* appears as a distinct form of FAAL (also called AasS)[65]. However, it seems likely that AasS is more related to ttFACS than FadD10 on the basis of sequence analysis[65]. Sequence alignment showed that AasS has 35.95% identity relative to ttFACS, much higher than that (22.07%) of FadD10 (Supplementary Fig. 2). To reveal the working mechanism of AasS, we carried out a series of studies with *V. harveyi* AasS.

To facilitate protein purification, we introduced a 6xHis-tag at the N terminus of AasS protein (Supplementary Fig. 4). In addition to long-chain FA species, such as oleate (Supplementary Figs. 5 and 6), we observed that the soluble AasS enzyme is active with the two atypical substrates, methyl-pimelic acid (M-pim or M-C7) and ethyl-pimelic acid (E-pim or E-C7), at the comparable level (Supplementary Fig. 7). Size-exclusion chromatography (SEC) analysis of the recombinant AasS protein (~60 kDa) revealed an apparent mass of ~380 kDa (Fig. 1a). This largely agreed with the calculated molecular weight (360–370 kDa) for AasS with analytical ultracentrifugation (AUC) (Fig. 1b). We showed that the solution structure of AasS hexamer is stable regardless of its varied concentration (Supplementary Fig. 8). On the contrary, Burgi et al. reported that yeast peroxisomal oxalyl-CoA synthetase exists in the dose-dependent conversion of oligomer (dimer–tetramer–hexamer)[68]. The hexameric AasS is also different from the dimeric FadD10 and ttFACS (Fig. 1a,b)[49,65]. The negatively stained sample forms a ring with a diameter of 15–20 nm (Fig. 1b). This verified an earlier observation that AasS forms higher-ordered aggregates[25]. Our gel filtration analysis revealed that its hexamer structure in solution remains unaltered even in the presence of 10 mM DTT (Supplementary Fig. 9), which stands in contrast to previous reports showing that the addition of 10 mM

Fig. 1 | Structural and functional definition of AasS hexamer. a, The SEC profile suggested that AasS behaves as a hexamer. A Superdex 200 increase column was applied here. The protein marker of gel filtration (GE HealthCare) was used to adjust this used column before separation of this recombinant AasS with an N-terminal 6xHis-tag, including (i) ferritin (440 kDa), (ii) aldolase (158 kDa) and (iii) BSA (~67 kDa). The N-terminal 6xHis-tagged version of AasS is predicted to be ~64 kDa. **b**, Use of AUC to determine the molecular mass of the recombinant AasS protein (~380 kDa). The inside graph denotes negative staining of AasS (0.02 mg ml^{-1}) and displays its solution structure of hexamer form. The protein particles in hexamer form are indicated with red arrows. **c**, Ribbon structure of AasS hexamer. **d**, The surface representation of AasS hexamer is labeled from I to VI. AasS_N domains are colored beige and hot pink, while AasS_C domains are colored light green and purple. **e**, Ribbon representation of an AasS protomer and monomer. **f**, Surface representations for AasS dimer and trimer interfaces. Each molecule of the AasS trimer arises from two neighboring dimers. AasS is composed of AasS_N (AasS′_N) and AasS_C (AasS′_C). **g**, Close-up views of the AasS dimer (and/or trimer) interfaces. Green dashed lines indicate hydrogen bonds or salt bridges. **h**, Use of in vitro enzymatic analyses to analyze the AasS dimer and trimer interfaces. **i**, Scheme for functional assays of AasS action in the biotin auxotrophic strain Δ*bioC*. **j**, Bacterial growth on M9 minimal medium was observed with E-pim as the sole carbon source. Bacterial viability combined with mutational analysis suggested that dimer (and/or trimer) formation of AasS is critical for enzymatic activity. The agar plates refer to M9 minimal medium with E-pim as the sole carbon source. M, protein marker. WT, wild type.

https://doi.org/10.1038/s41594-024-01464-7

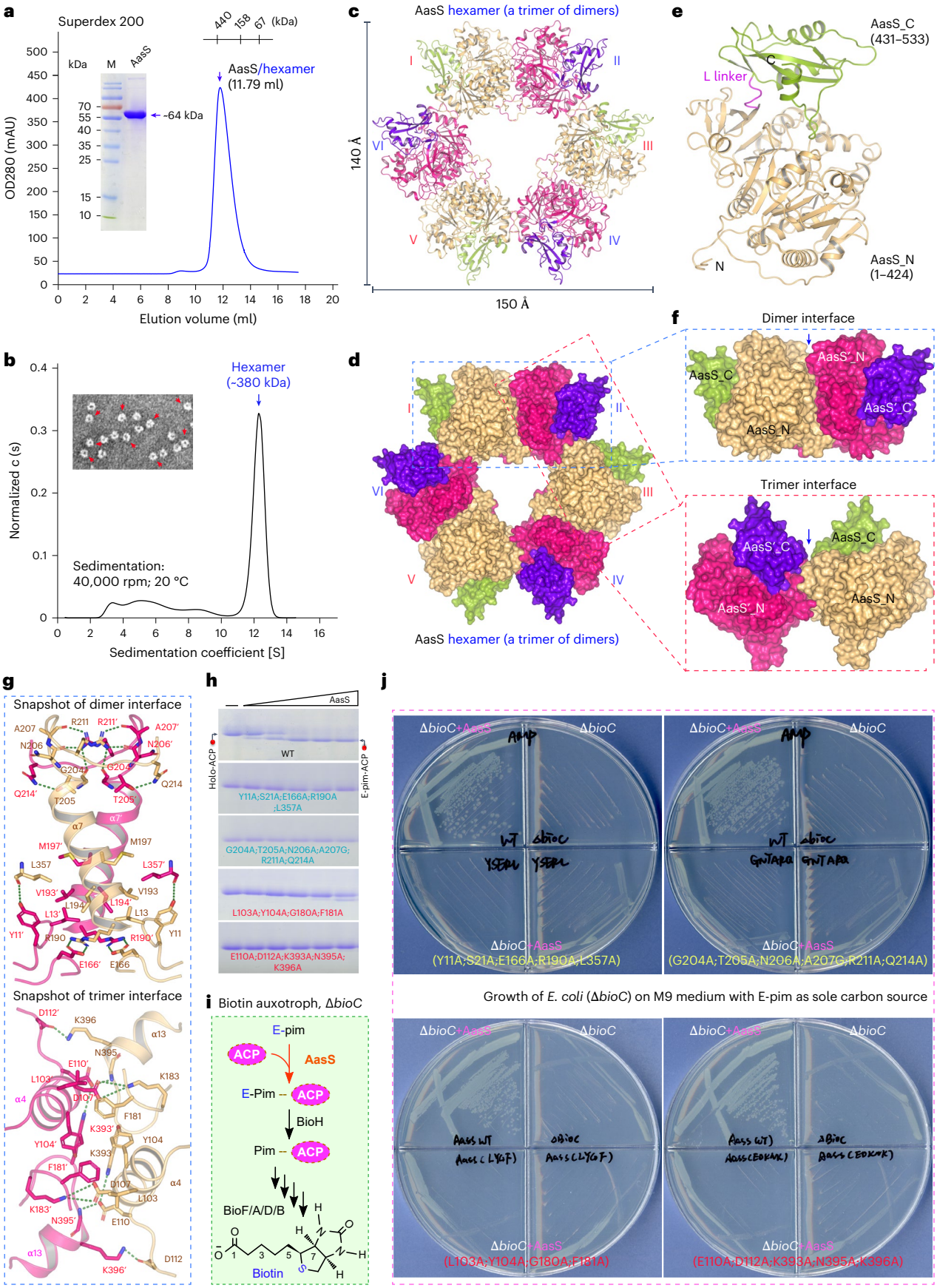

https://doi.org/10.1038/s41594-024-01464-7

Table 1 | Cryo-EM data collection, refinement and validation statistics

Macromolecule	AasS								
Ligands	**None (PDB 8HZX)**	**AMP-PNP (PDB 8I3I)**	**ATP (PDB 8I49)**	**E-C7 (PDB 8I22)**	**C18:1 (PDB 8I35)**	**M-C7-AMP (PDB 8I51)**	**C18:1-AMP (PDB 8I6M)**	**M-C7-ACP (PDB 8I8D)**	**C18:1-ACP (PDB 8I8E)**
Mg^{2+}	–	+	–	–	–	+	+	–	–
Data collection and processing									
Magnification	29,000	29,000	29,000	130,000	29,000	29,000	29,000	29,000	29,000
Voltage (kV)	300	300	300	300	300	300	300	300	300
Electron exposure (e^- per Å^2)	78	78	78	52	78	78	78	78	78
Defocus range (μm)	−1.5 to −2.5	−1.5 to −2.5	−1.5 to −2.5	−0.6 to −1.5	−1.5 to −2.5	−1.5 to −2.5	−1.5 to −2.5	−1.5 to −2.5	−1.5 to −2.5
Pixel size (Å)	1.014	1.014	1.014	0.93	1.014	1.014	1.014	1.014	1.014
Symmetry imposed	*D3*	*D2*	*D3*	*D3*	*D3*	*D3*	*D3*	*D3*	*D3*
Initial particle images	772,681	1,065,909	1,768,321	2,109,261	968,887	905,237	799,666	2,481,529	1,540,255
Final particle images	213,572	282,818	419,290	510,518	217,323	199,919	337,562	247,748	299,233
Map resolution (Å)	2.68	2.68	2.45	2.17	2.79	2.77	2.61	2.53	2.70
Refinement and validation									
Root-mean-square deviation									
Bond lengths (Å)	0.007	0.007	0.015	0.007	0.006	0.012	0.008	0.007	0.004
Bond angles (°)	1.081	1.137	1.635	1.036	1.136	1.332	1.138	1.187	0.641
MolProbity score	1.90	1.83	1.83	1.74	2.05	2.03	2.01	1.78	2.02
Clash score	8.72	6.77	7.48	8.41	10.48	9.96	9.71	7.90	9.89
Poor rotamers (%)	0.00	0.44	0.43	0.65	0.29	0.69	0.80	0.76	0.76
Ramachandran plot									
Favored (%)	93.37	92.66	93.75	95.93	91.16	91.32	91.63	94.89	91.64
Allowed (%)	6.44	7.14	6.06	3.88	8.65	8.49	8.17	5.11	8.19
Disallowed (%)	0.19	0.19	0.19	0.19	0.19	0.19	0.19	0.00	0.17

The '+' denotes the presence of Mg^{2+} and '–' denotes its absence.

DTT renders the conversion of AasS from ordered oligomer to monomer[25]. To address the question of the oligomeric state of AasS, we used cryo-EM to investigate its architecture (Fig. 1 and Extended Data Fig. 1).

Overall structure of AasS hexamer

In total, we obtained nine sets of AasS cryo-EM structures: AasS alone (apo) and eight complexes generated after incubation of the enzyme with its cofactors, substrates, intermediates and final products (Table 1 and Supplementary Figs. 10 and 11). In addition to its architecture (Extended Data Fig. 1), the relatively high resolution of the single-particle reconstructions (2.17–2.77 Å) enabled visualizing the bound ligands (substrates or products) and conformational changes of critical residues for AasS function (Table 1 and Supplementary Figs. 12–15). We determined the structure of the apo form at 2.68-Å resolution (Extended Data Fig. 1). The apo-AasS structure forms a ring-like hexamer with dimensions of approximately 140 × 150 × 80 Å^3 (Fig. 1c,d). Like other AAE members, each subunit of AasS hexamer exhibits a 'hammer-and-anvil' model, folding into two distinct domains: a large N-terminal domain (residues 1–424), called AasS_N, and a compact lid domain at the C terminus (residues 431–533), termed AasS_C. The two domains are connected by a six-residue linker (Fig. 1e). The AasS_N domain consists of three β-sheets flanked by α-helices and adopts a pitcher-like shape, whose central place constitutes a putative substrate-binding cavity. The AasS_C domain contains two β-sheets (one two-stranded β-sheet (β20-β21) and one three-stranded β-sheet (β22-β23-β24)) surrounded by three α-helices (α16-α17-α18), hovering on the top of putative active sites within the AasS_N domain (Supplementary Fig. 16). The structure of individual AasS protomer is similar to that of ttFACS with two separated domains (Supplementary Fig. 17). Structural comparison suggested that the apo-AasS_C domain displays an adenylate-forming conformation (Fig. 1e)[69].

Earlier studies showed that the N-terminal domain leads to homodimerization for adenylation-executing enzymes (Supplementary Fig. 18). Thus, we designated the AasS hexamer as a trimer of dimers (Fig. 1c–f). The oligomerization of AasS is mainly driven by two unique interfaces, the dimer interface and the trimer interface, and both are formed by AasS_N/AasS′_N domains (Fig. 1d,f). The dimer interface is formed by α7/α7′ helices and a few surrounding loops (Fig. 1g). At the top region, the residue R211/R211′ forms hydrogen bonds with the main groups of three residues (A207′/A207, N206′/N206 and G204′/G204); in the middle part, four hydrophobic residues (L13/L13′, M197/M197′, L194/L194′ and Y11/Y11′) pack together; at the bottom, the basic R190/R190′ electrostatically interacts with the acidic residue E166′/E166. The trimer interface is mediated by two kinds of interactions, hydrophobic interactions (F181, Y104 and L103) in the middle and polar interactions formed by a number of residues (K396, N395, K393, E110, K183, D107 and D112) at the bottom (Fig. 1g). Next, we constructed four AasS mutants to address the roles of the dimer and trimer interface residues (Supplementary Table 1). Amino acid substitution of interface residues impaired AasS oligomerization (Supplementary Fig. 19). All the AasS mutants failed to transfer E-pim substrate to the acceptor holo-ACP in our enzymatic assay (Fig. 1h). Given the fact that E-pim-ACP is a surrogate substrate for the late stage of biotin synthesis and that the *E. coli* Δ*bioC* strain is a biotin auxotroph whose primary biotin step is impaired, expression of active AasS presumably enables the Δ*bioC* strain to bypass the need of biotin cofactor upon exogenous E-pim as a carbon source (Fig. 1i). Thereafter, we performed the Δ*bioC* indicator-based bioassay for AasS activity as established by Lin and

Cronan (Fig. 1i,j)[70]. Indeed, the wild-type AasS did render viability of the biotin-requiring strain on the nonpermissive condition containing E-pim (Fig. 1j). Notably, none of the four AasS derivatives enabled the appearance of the biotin auxotroph on the biotin-lacking condition. Cryo-EM study-guided data constitute structural and functional proof for the AasS hexamer.

Recognition of AasS by ATP or AMP-PNP (adenylyl-imidodiphosphate) cofactor

To elucidate how AasS recognizes the ATP cofactor, we determined two complex structures. The AasS protein (~0.3 mM) was incubated with 1.5 mM ATP to give the ATP-liganded AasS complex. In the presence of 2 mM $MgCl_2$, AasS (~0.35 mM) was mixed with AMP-PNP, the nonhydrolyzable ATP analog, producing the tripartite complex of AasS–AMP-PNP–Mg^{2+}. The homogeneity of the negatively stained samples was observed by EM (Extended Data Fig. 2a) and then the samples were vitrified with liquid ethane. Before the freezing procedure (Supplementary Fig. 10), both samples were subjected to treatment with 2 mM Fos-choline 8. Reconstruction from the cryo-EM dataset of AasS liganded with AMP-PNP analog (Fig. 2a,c and Extended Data Fig. 3) showed continuous density for the bound AMP-PNP cofactor (Fig. 2c,e and Supplementary Figs. 14 and 15). In brief, the adenine base of AMP-PNP inserts into a hydrophobic pocket formed by a number of residues such as Y318 and A298 (Fig. 2c–e). Additionally, its amino group forms a hydrogen bond with the G317 main chain carbonyl oxygen (Fig. 2e). The pentose sugar hydroxyl group of AMP-PNP forms a hydrogen bond with the AasS D411 residue and the α-phosphate is stabilized by the two residues of the AasS_N domain (S321 and H226) and K522 from the AasS_C domain (Fig. 2c–e). The β-phosphate of the AMP-PNP ligand is coordinated by the two sites (R426 and T178) and the γ-phosphate interacts with the side chains of the three residues, T178, T175 and K183 (Fig. 2e). In addition, a Mg^{2+} ion is positioned between the β-phosphate and γ-phosphate groups, which facilitates neutralizing the negative charges. From the cryo-EM data for AasS-liganded with ATP, we note that the Mg^{2+} ion was omitted during sample preparation to prevent ATP hydrolysis. In agreement with the result from the negatively stained sample without $MgCl_2$ (Extended Data Fig. 2), the cryo-EM structure of ATP-liganded AasS remains a hexamer ring (Supplementary Fig. 12). The cryo-EM densities for the phosphate groups are visible but not continuous (Fig. 2d,f and Supplementary Figs. 14 and 15). Accordingly, in the AasS–ATP structure, the conformation of the P-loop, which is involved in coordinating ATP phosphate groups along with the Mg^{2+} ion, is similar to the apo structure. This is generally consistent with the proposal of Andreini et al. that the Mg^{2+} ion binds to ATP[71]. Thus, it seemed likely that the Mg^{2+} ion is required for the P-loop to adopt a similar conformation to that seen in the AasS–AMP-PNP–Mg^{2+} complex structure (Extended Data Figs. 4 and 5).

To probe the function of ATP and AMP-PNP recognition residues, we created four AasS single mutants (T178A, K183A, Y318A and E322A) (Supplementary Table 1). Except for the AasS(K183A) mutant that retained some poor activity, none of the remaining three derivatives (T178A, Y318A and E322A) was active in using E-pim in vitro (Fig. 2g). Subsequently, we analyzed the varied abilities of AasS mutants in vivo (Figs. 1i and 4e). The K183A mutant of AasS only conferred mild growth of the Δ*bioC* strain in biotin-deficient M9 medium. The T178A mutant seemed next to the K183A mutant in allowing the growth of the Δ*bioC* indicator strain (Fig. 2h,i). Moreover, a single substitution of either Y318 or E322 markedly abolished enzymatic activity of AasS in vivo (Fig. 2h,i). Notably, all the plasmid-borne *aasS* derivatives were verified by western blot to express at a comparable level (Fig. 2i). This ruled out the possibility that the loss of AasS function was attributed to its altered expression. Therefore, our results illustrate a functional pocket through which AasS recognizes its ATP or AMP-PNP ligand (Extended Data Fig. 6a–d).

The AasS tetramer is a catalysis intermediate

The negative-staining EM analysis revealed a number of hexamer particles formed by AasS protein (0.02 mg ml^{-1}) regardless of whether its cofactors ATP (or its non-metabolizable substance AMP-PNP) and $MgCl_2$ were present (Extended Data Fig. 2a). Coexistence of $MgCl_2$ and ATP or its AMP-PNP analog triggered the emergence of AasS tetrameric particles along with its ancestral hexamer (Extended Data Fig. 2a,b). In fact, the concentration of Mg^{2+} supplemented in our assays in vitro was comparable to the cytosolic level at 2 mM in *E. coli*[72]. From hundreds of micrographs collected from negatively stained EM samples, two-dimensional (2D) classification suggested the occurrence of a substantial number of tetrameric AasS particles. The relative ratio of tetramer to hexamer was around 1.5:1 (Extended Data Fig. 2c). Therefore, it raised the possibility that ATP (or its analog AMP-PNP) and Mg^{2+} trigger the conversion of the AasS tetramer from its stable hexamer state regardless of acyl substrates. A similar scenario was seen with a DNA-unwinding enzyme called HerA[73]. The HerA enzyme dominates as a heptamer, which is converted to a hexamer upon binding to ATP and its analog AMP-PNP[73]. Next, we collected two cryo-EM datasets for AasS with ATP alone or $MgCl_2$ and AMP-PNP (Table 1). Indeed, the complex of AasS with $MgCl_2$ and AMP-PNP adopted a tetramer arrangement (Extended Data Fig. 3). The overall architecture could be regarded as a dimer of dimers with dimensions of about 110 × 110 × 80 $Å^3$ (Fig. 3a,b). Unlike the C-terminal domain of ttFACS that undergoes a certain conformational transition from an open state to a closed state upon AMP-PNP binding (Extended Data Fig. 4a–d), the AasS_C domain remains in the open conformation even in the presence of AMP-PNP (Extended Data Fig. 4e–h). This is partially attributed to direct contact between AMP-PNP and ttFACS, whereas this is not the case in AasS (Extended Data Fig. 5a–d). As for the tetrameric intermediate, the first dimer interface (Fig. 3c,d) is identical to that of the apo-AasS dimer (Fig. 1f,g). The second dimer interface of the AasS tetramer involves a group of similar residues (K393, E110 and N395; Fig. 3e,f) to the aforementioned trimer interface of the AasS hexamer but the specific arrangement is quite different (Fig. 1f,g). In addition, K399/K399′ interacts with D64′/D64 electrostatically in the AasS tetramer (Fig. 3f).

To determine the mechanism of AasS transition from hexamer to tetramer, we investigated its monomeric structure liganded by $MgCl_2$ and AMP-PNP, which was superimposed on the trimer interface of the hexamer form (Fig. 3g). We discovered two residues (F181 and K183) with substantial movement, which was because of the co-occurrence of $MgCl_2$ and AMP-PNP (Fig. 3g). In the AasS hexamer, the residue K183 interacts with the D107′ residue from the other AasS molecule.

Fig. 2 | Structure–function analyses for the interplay between AasS and ATP or AMP-PNP. a, Chemical structure of AMP-PNP analog. **b**, Structural illustration for ATP molecule. **c**, Surface representation of the substrate cavity of AasS bound to AMP-PNP, a nonhydrolyzable ATP analog. **d**, Cut-away view of the ligand cavity of AasS with ATP bound. **e**, Close-up view of key residues interacting with AMP-PNP. The sites coordinating AMP-PNP are displayed as sticks, while yellow dashed lines denote hydrogen bonds or salt bridges. **f**, Structural snapshot for potential ATP-coordinating residues. The putative sites coordinating ATP are displayed as sticks, while yellow dashed lines denote hydrogen bonds. The presence of $MgCl_2$ (green sphere) is given as 'w/ $MgCl_2$' (**c**,**e**), whereas its absence is shown as 'w/o $MgCl_2$' (**d**,**f**). **g**, Comparison of enzymatic activities of the four AasS mutants (T178A, K183A, Y318A and E322A). **h**, The abilities of the four AasS mutants (T178A, K183A, Y318A and E322A) differ in allowing the growth of Δ*bioC* on M9 minimal agar plates with E-pim as the sole carbon source. **i**, Growth curves of the biotin auxotrophic strain Δ*bioC* carrying certain AasS mutants in M9 minimal medium with E-pim as the sole carbon source. The growth curve is given as the mean values ± s.d. from three independent experiments. The inside gel denotes western blot-based analysis of the expression of the four AasS mutants in the Δ*bioC* recipient strain before the functional assays.

https://doi.org/10.1038/s41594-024-01464-7

However, in the AasS tetramer, the residue K183 rotates by 180° and interacts with the γ-phosphate of the nonhydrolyzable ATP analog AMP-PNP (Extended Data Fig. 5a–h). In contrast, no similar scenario was seen with the ttFACS dimer (Extended Data Fig. 5b). This might explain why the ATP analog, AMP-PNP, stimulates the formation of AasS tetramer in the presence of $MgCl_2$. Then, we created several AasS tetramer-related mutants (Supplementary Table 1). Among them, the two derivatives of AasS (K183A and D107A;K183A) migrated slower in gel filtration analysis when compared to the parental type (Fig. 3h). This indicated that they were necessary for conformational maintenance of the tetramer or hexamer.

Loading of FAs by AasS

To address how FAs are loaded by the AasS hexamer, we prepared enzyme complexes liganded with E-pim or C18:1 for cryo-EM investigation (Supplementary Fig. 10d,e). As a result, cryo-EM structures

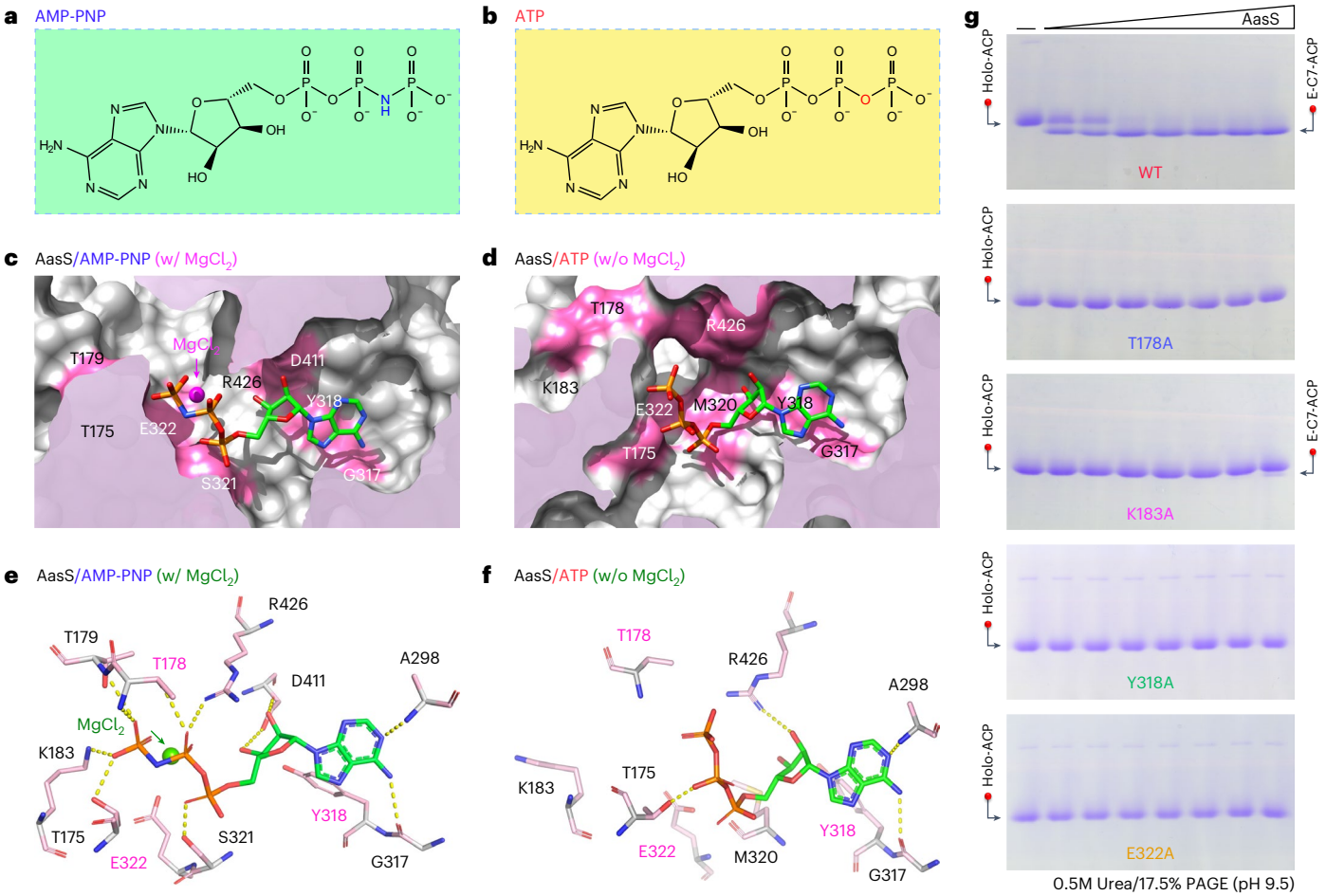

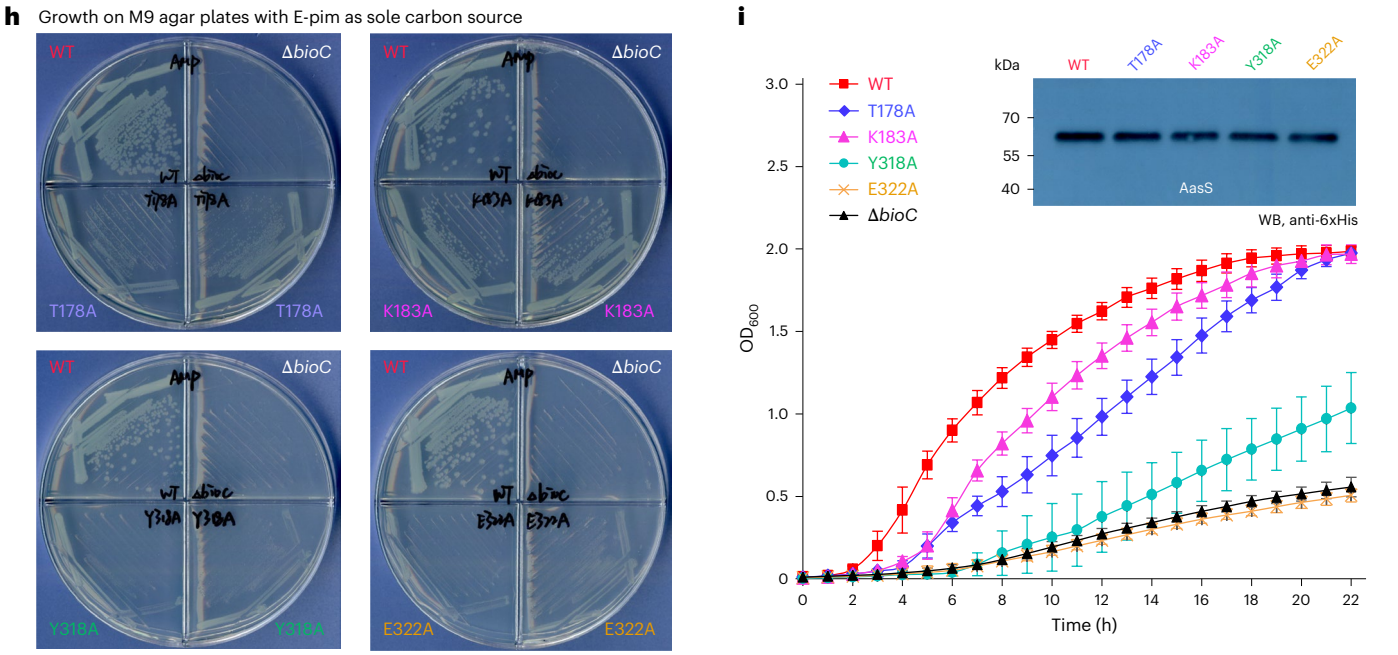

https://doi.org/10.1038/s41594-024-01464-7

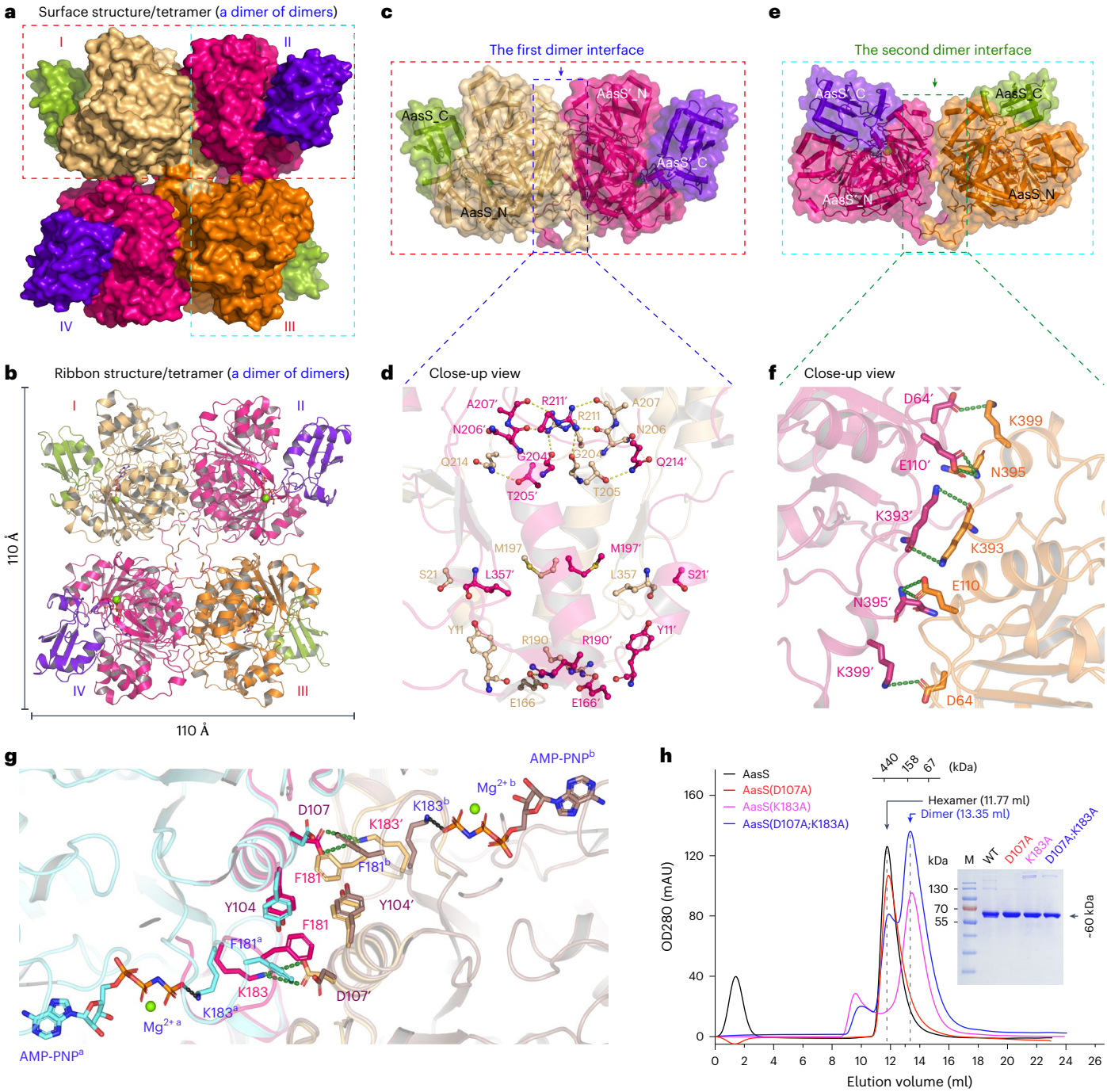

Fig. 3 | Discovery of AasS tetramer, a catalysis intermediate. a,**b**, Surface illustration (**a**) and ribbon structure (**b**) for AasS tetramer triggered by an ATP analog (AMP-PNP) and $MgCl_2$. The tetrameric AasS intermediate appears as a dimer of dimers. The protomer of AasS tetramer is numbered from I to IV. **c**, Surface representation for the dimeric subunit of AasS enzyme. The first dimer interface is indicated with a blue arrow. **d**, Close-up view of the first dimer interface of AasS tetramer. **e**, Structural snapshot for an interplay between the two AasS dimer subunits. The second dimer interface is shown with a green arrow. **f**, Close-up view of the second dimer interface of AasS tetramer. The putative hydrophobic bond-forming residues are given. **g**, Two AasS monomers (colored cyan and chocolate) with Mg^{2+} and AMP-PNP bound superimposed on the trimer interface of the hexamer (colored hot pink and beige). Because of the presence of Mg^{2+} and AMP-PNP, two residues (K183 and F181) moved substantially. K183 interacts with D107 in the hexamer, whereas it rotates by 180° in the tetramer and interacts with the γ-phosphate of AMP-PNP. This explains why AasS with Mg and AMP-PNP bound appears as a tetramer. **h**, Gel filtration analyses for the functional roles of two residues (D107 and K183) in the maintenance of AasS organization. To compare the molecular weight of AasS and its mutants, the standard of gel filtration was applied using (i) ferritin (~440 kDa), (ii) aldolase (~158 kDa) and (iii) BSA (~67 kDa). The 6x His-tagged AasS at the N terminus is estimated to be ~64 kDa. It suggested that the K183A substitution disrupts the conformational maintenance of the AasS hexamer (or tetramer).

were refined to 2.17 Å for AasS–E-pim and 2.79 Å for AasS–C18:1 (Table 1 and Supplementary Figs. 11c–f and 12d, e). The two complexes also form a ring-shaped hexamer and each subunit carries a molecule of E-pim or C18:1 (Extended Data Fig. 6e–h). In the complex structures, the FA-binding pockets mainly locate within the AasS_N domain (Extended Data Fig. 6). Several hydrophobic residues (for example, W230 and V227) inside the substrate cavity efficiently prevent the exposure of ACP-linked acyl chains to solvents during AasS catalysis (Fig. 4a–d

and Extended Data Fig. 6e–h)[15]. Given the chain-flipping mechanism that is assigned to FAS II enzymes with an acyl-ACP as substrate[8,15], we provisionally termed this opposite process as the reversal of the chain-flipping mechanism. The FA-binding pocket appears as a tunnel featuring two open ends on the ttFACS surface[49]. Relative to the first opening that intersects with the so-called ATP path, the second opening occurs in the bottom of ttFACS_N domain. However, the AasS substrate-loading cavity is a unidirectional hole retaining a single opening, equivalent to the first one of ttFACS. This is because the region in AasS_N corresponding to the second opening of ttFACS is consistently closed across all nine AasS structures we report here (Table 1 and Supplementary Figs. 12–15). In contrast to ttFACS that loads acyl substrates through its second entrance site (Supplementary Fig. 20)[49], AasS presumably captures FAs through the only entrance (Extended Data Fig. 6e–l), unless an alternative or unknown entrance is formed. Because the ATP-binding site is also situated at the entrance to the hole, we anticipated that AasS can load FAs only before ATP binding.

Binding of AasS to acyl-AMP intermediates

In terms of the intermediates produced in the AasS 'first-half' reaction, we prepared two kinds of acyl-adenylates: M-pim-AMP and oleoyl (C18:1)-AMP. Overall structures of the two resultant AasS and acyl-AMP complexes were separately refined to 2.77 Å for AasS–M-C7-AMP, and 2.61 Å for AasS–oleoyl-AMP (Table 1 and Supplementary Figs. 11–15). The two structures adopt a similar architecture to apo-AasS, except for the residues coordinating acyl-AMP intermediates (Fig. 4a–d and Supplementary Fig. 20). The V-shaped acyl-AMP adenylates fit into a branched cavity inside the AasS_N domain (Fig. 4a,c). Clearly, the carbon chain of both M-pimelic and oleoyl moieties is accommodated by a long hydrophobic tunnel (Fig. 4a,c). Structural analyses suggested that both the adenine base and sugar are in a similar position to AMP-PNP (Figs. 2a–f and 4b–d). In particular, residue R426 that interacts with the β-phosphate of AMP-PNP (Fig. 2c–f) now forms a hydrogen-bond network with the sugar hydroxyl groups (Fig. 4b–d and Extended Data Fig. 6i–l). The α-phosphate is coordinated by a Mg^{2+} atom and the hydroxyl groups of S321 and T175. The Mg^{2+} ion is held in place by the negatively charged E322 (Fig. 4b–d and Extended Data Fig. 6j). The carbonyl group of oleoyl-AMP forms a hydrogen bond with residue H226 (Extended Data Fig. 6l). The first half of the oleic acid moiety is fixed in place by the conserved W230 (Extended Data Fig. 6k,l), which is equivalent to W234 of ttFACS gatekeeping FA entry (Fig. 6a–d)[49]. A similar scenario was also seen with the cavity bound by the M-pim-AMP intermediate.

Next, we evaluated critical roles of the residues in coordinating acyl-AMP intermediates. Totally, we generated 12 AasS mutants (Supplementary Table 1). In addition to enzymatic assays with the recombinant AasS derivatives (Supplementary Fig. 21), the experiments of genetic complementation were integrated (Supplementary Fig. 22). The expression profiles of these mutants were validated by western blot before functional analyses (Supplementary Fig. 22a,b). Additionally, we examined the in vivo roles of these residues by assaying the varied level of AasS-aided viabilities of Δ*bioC* reporter strains (Fig. 4e). This idea was confirmed by the fact that AasS catalyzes E-pim-ACP formation, bypassing the requirement of BioC's initial step of DTB and biotin synthesis in the reconstituted system in vitro (Fig. 4f). Except for the K465A substitution with no detectable role, the 11 other AasS mutants were functionally defective (Supplementary Fig. 22c,d). In addition to the double and triple mutants, three single mutants (T175A, S321A and K522A) almost completely lost function in vitro and in vivo. Given that the majority of FAS II enzymes transiently interact with fatty acyl substrates, we were fortunate to capture the binding of E-pim to AasS (in the presence of cofactor ATP) in our isothermal titration calorimetry (ITC). The stoichiometry (n) was ~0.85, close to its theoretical value of 1.0 (Fig. 4g). The dissociation constant (K_d) value of ~6.45 μM suggests a modest affinity of the AasS enzyme for E-pim substrate (Fig. 4g). Collectively, characterization of the AasS and acyl-AMP intermediates offer insights into the catalytic mechanism for eFA recycling.

Architecture of AasS and acyl-ACP complex

As Cronan and Rock previously described with AasS and AasC action[52,74,75], both M-pim-ACP and oleoyl-ACP substances were prepared here. In brief, we used AasS enzyme to ligate M-pim (and/or oleate) FA with holo-ACP, an activated form of ACP species. As a result, this generated M-pim-ACP (oleoyl-ACP) thioesters. Following the treatment of isopropanol, the purified products (M-pim-ACP (~0.7 mM) and oleoyl-ACP (~0.2 mM)) were separately subjected to an incubation with AasS (~0.3 mM) and gave two complexes of AasS–M-pim-ACP and AasS–oleoyl-ACP accordingly. Although the reconstruction of cryo-EM datasets presented a relatively weak but discernable density for the partner ACP-Ppan–oleic acid (or ACP-Ppan–M-pim) and its byproduct AMP (Extended Data Figs. 6 and 7 and Supplementary Figs. 14 and 15), overall structures of AasS in complex with M-pim-ACP or oleoyl-ACP were determined at 2.53 Å and 2.70 Å, respectively. Not surprisingly, both of them form a ring-shaped heterohexamer with dimensions of 160 × 170 × 80 $Å^3$ for AasS–M-pim-ACP (Fig. 5a–d) and 160 × 180 × 80 $Å^3$ for AasS–C18:1-ACP (Extended Data Fig. 8a–d). Each protomer carries one acyl-ACP subunit, the ACP group of which is mostly bound by the AasS_C domain (Fig. 5a–f and Extended Data Fig. 7a–d). Our ITC assay determined modest affinity of AasS for its partner ACP, for which the stoichiometry was ~1.3 (Fig. 5g). This agreed with the structural organization of AasS complexed with two types of acyl-ACP products (Fig. 5 and Extended Data Fig. 8). Similar to most AasS structures we solved (seven of eight), the C-terminal domain adopts an open conformation to accommodate the C18:1-ACP product (Extended Data Fig. 7)[46,63,76], whereas, for the M-pim-ACP partner, the AasS_C domain is transformed into the closed conformation (Extended Data Fig. 7 and Supplementary Fig. 23)[69,76,77]. Indeed, the AasS_C domain in the M-pim-ACP–AasS complex is rotated by ~154° (Fig. 7a, Extended Data Fig. 7 and Supplementary Fig. 24), as observed for 4-chlorobenzoate:CoA ligase (CBL) with the C-terminal domain rotated ~140° between adenylate-forming and thioester-forming conformations[69].

In the AasS–M-pim-ACP complex, the negatively charged and hydrophobic residues of ACP α3 and α4 helices complement with the positively charged and hydrophobic surface on the AasS_C domain

Fig. 4 | Structural and functional insights into the acyl-AMP intermediate formation by AasS. a, Cut-away view of the cavity of AasS occupied by the M-pim(C7)-AMP intermediate. **b**, Putative residues of AasS that coordinate M-pim(C7)-AMP. These residues are displayed as sticks, while yellow dashed lines denote hydrogen bonds. **c**, Enlarged view of the substrate cavity of AasS recognized by the oleoyl(C18:1)-AMP intermediate. **d**, Putative residues of AasS implicated into its oleoyl-AMP binding. **e**, The rationale for the in vivo assay of AasS activity with the biotin auxotrophic strain Δ*bioC*, growing on nonpermissive M9 minimal medium with E-pim as the sole carbon source. **f**, The biotin bioassay demonstrated that AasS synthesizes E-C7-ACP, bypassing the initial BioC-catalyzed step of malonyl-ACP methyl ester formation in vitro. Left: scheme for AasS-circumvented DTB and biotin synthesis reconstituted in vitro. The positive control denotes biotin added on a paper disc (1–6 pmol), whereas the negative control refers to biotin-free Δ*bioC* extract (~20 μl). AasS was used to generate E-pim-ACP. The Δ*bioC* extract-based reaction mixtures (from 5 to 20 μl) were spotted on paper discs to probe whether or not DTB and biotin production occurred in vitro. The biotin auxotroph ER90(Δ*bioF*/*C*/*D*) functioned as a reporter strain[14,82]. Presence of DTB or biotin allows bacterial viability of the ER90 strain, displaying an insoluble red pigment precipitated around the paper disc through the reduction of 0.01% TTC. **g**, Use of ITC to probe transient binding of E-pim to AasS enzyme in the presence of ATP. The values of n and K_d are given as the means ± s.d. of three independent trials. BioF, 7-keto-8-aminopelargonic acid synthase; BioA, 7,8-diaminopelargonic acid synthase; BioD, dethiobiotin synthase; BioB, biotin synthase; DP, differential power.

https://doi.org/10.1038/s41594-024-01464-7

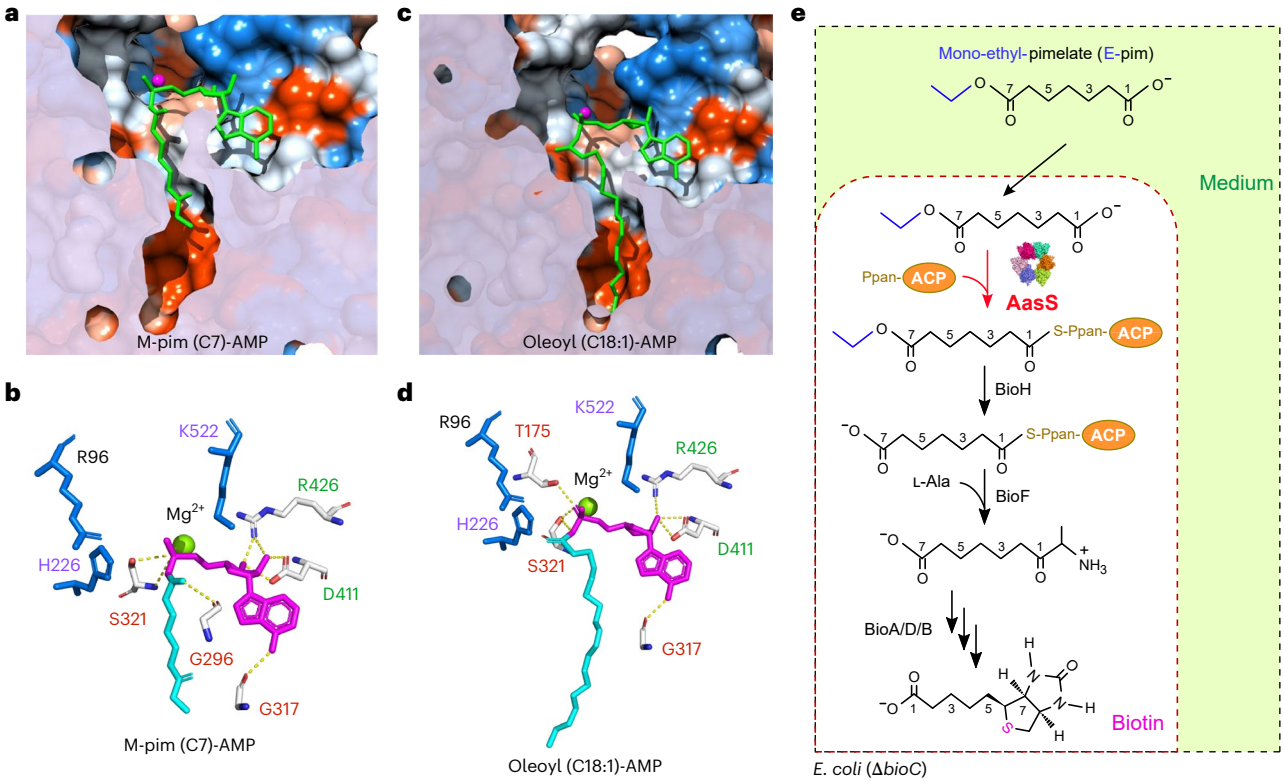

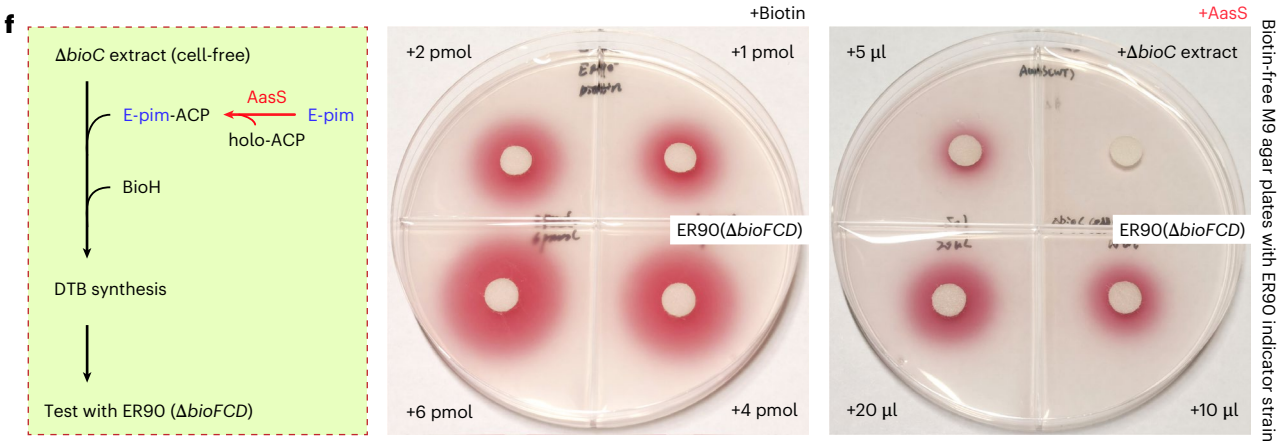

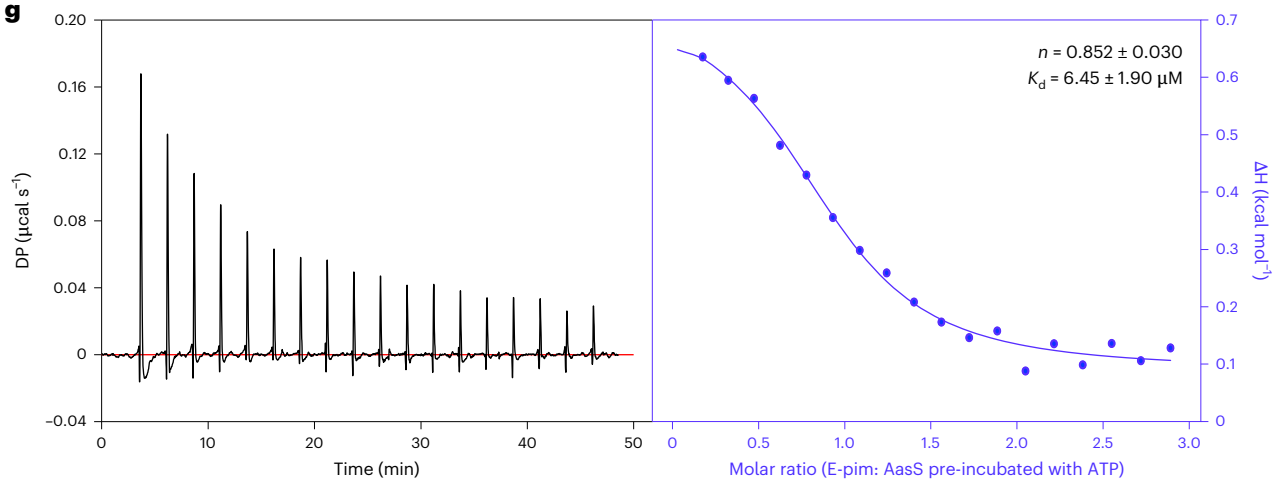

https://doi.org/10.1038/s41594-024-01464-7

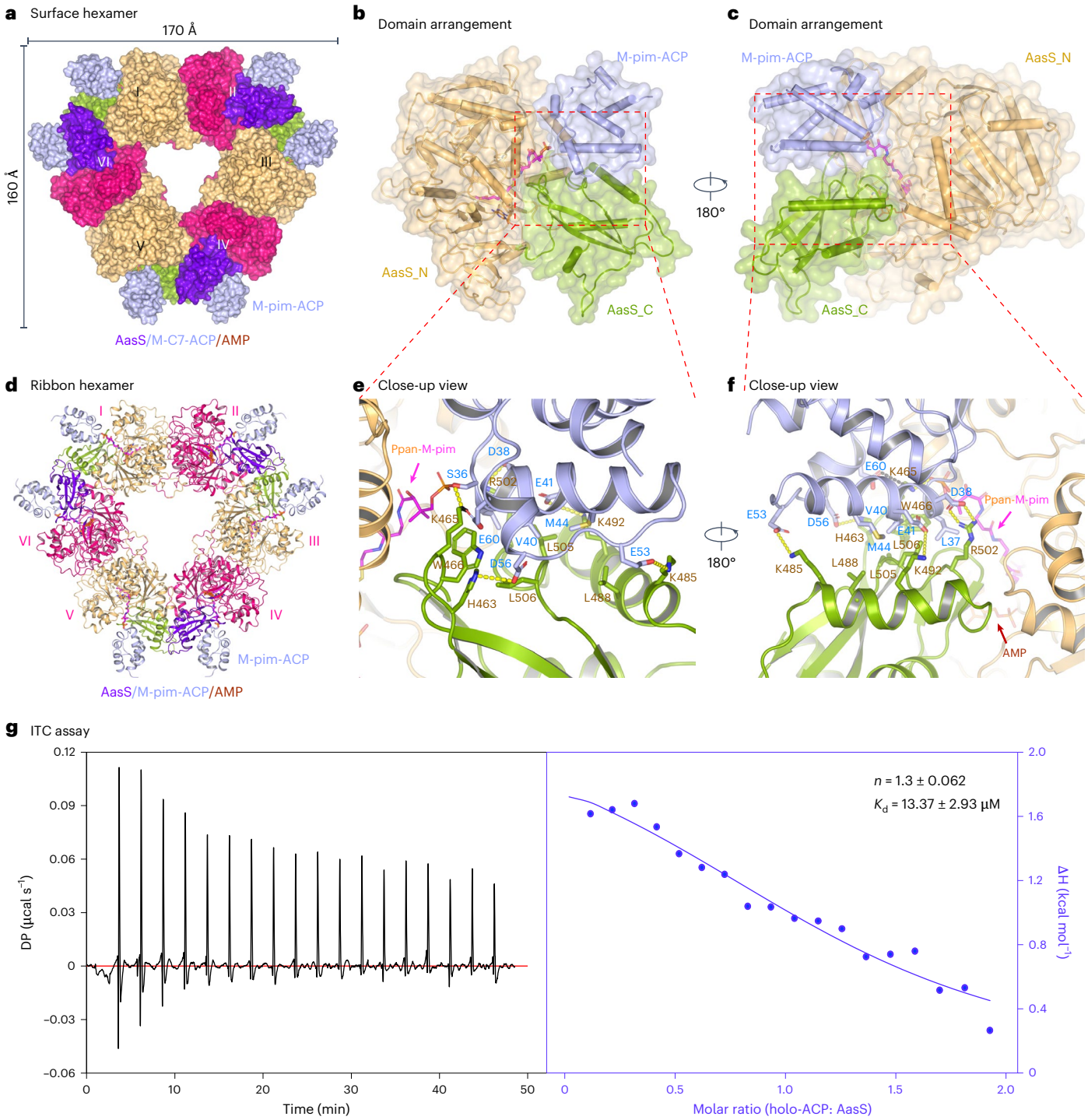

Fig. 5 | Probing the interplay between AasS and its acyl-ACP substrate. **a**, Surface representation of AasS–M-pim-ACP hexamer. **b**, Surface presentation for domain arrangement of one AasS in complex with M-pim-ACP. **c**, Structural snapshot for domain arrangement of one AasS–M-pim-ACP complex (**b**) with counterclockwise rotation of 180°. **d**, Cartoon representation of AasS–M-pim-ACP hexamer. Each protomer of the hexameric AasS–M-pim-ACP complex is labeled from I to VI. **e**, Close-up view of an interface between AasS and its product M-pim-ACP. **f**, Enlarged view of AasS–M-pim-ACP interface (**e**) rotated 180° counterclockwise. As shown in **e** and **f**, the AasS–M-pim-ACP interfaces are defined to comprise two kinds of interactions: (i) electrostatic (negatively charged residues from ACP are paired with positively charged residues from AasS_C domain) and (ii) hydrophobic (V40, M44 and L37 from ACP packs with W466, L506, L505 and L488 from AasS_C subunit; K465 also interacts with S36 and the Ppan moiety). **g**, The ITC assay for binding of AasS to its cognate ACP moiety. The values of n and K_d are given as the means ± s.d. of three independent trials.

(Fig. 5b,c). Specifically, five acidic residues of ACP (E53, D56, D38, E41 and E60) form salt bridges or hydrogen bonds with the five basic sites (K465, H463, K485, K492 and R502) of the AasS_C domain (Fig. 5e,f). Additionally, three residues (L37, V40 and M44) in ACP might interact with hydrophobic amino acids (W466, L506, L505 and L488) in AasS_C domain. The ACP–AasS_C association buries an area of ~540 Å^2. As for the C18:1-ACP–AasS complex, the situation of AasS_C is unaltered and its ACP partner makes a few contacts with the AasS_C domain: (1) D56 and E57 interacts with K477; (2) Y71 and E53 form several hydrogen bonds with E478 and Q481 (Extended Data Fig. 8e,f); and (3) the

ACP–AasS_C association buries an area of 474 Å^2 (Supplementary Fig. 25). The pattern of AasS–acyl-ACP interplay is similar to that of the BioH–M-pim-ACP complex (Supplementary Fig. 26). Unlike the oleoyl-ACP–AasS structure that represents a late stage after oleoyl-ACP conjugation, the M-pim-ACP–AasS structure suggests a more stabilized conformation of the acyl-ACP product (Fig. 7). It should be noted that AasS treats M-pim-ACP (or oleoyl-ACP) as a product rather than a reactant. Upon dissociation with AasS, the fatty acyl chains are resequestered by the helix bundle in ACP. This proceeds through an allosteric mechanism called chain flipping, which benefits the efficient access of fatty acyl thioesters and proximal carbon atoms without any exposure to solvents[12,15].

Because the structures of AasS in complex with its products, M-pim-ACP and C18:1-ACP, informed us that its C-terminal domain is a partner of the acyl-ACP product (Extended Data Fig. 9a,b), we hypothesize that AasS_C is indispensable for AasS function. The C-terminal domain deletion version of AasS(ΔC) we produced was functionally defective in the enzymatic assays (Extended Data Fig. 9c,d). Moreover, the C-terminal domain's removal disabled AasS to support growth of the Δ*bioC* strain in biotin-lacking conditions (Extended Data Fig. 9e). The combined data verify the essentiality of the C-terminal domain for AasS activity. In particular, unlike the single S434A mutant that was indistinguishable from the wild type (Supplementary Fig. 27), both the triple mutant (K485A;K492A;R502A) and the double mutant (K465A;W466A) were inactive (Extended Data Fig. 10a,b). This highlights that the aforementioned positively charged residues have synergistic roles in AasS binding acyl-ACP partners.

A gating role of W230 in AasS catalysis

As for the apo-ttFACS structure, the W234 residue is considered as a gatekeeper, where the indole ring is right in the middle of the FA-binding tunnel (Fig. 6a)[49]. Binding of the ligand AMP-PNP results in marked alteration of W234 orientation, designated as an open conformation, relative to that of apo-ttFACS (Fig. 6b)[49]. A similar scenario was seen with the ttFACS complexed with its intermediate C14:0-AMP adenylate, in which the ring nitrogen of W234 packs against the C14 moiety of C14:0-AMP (Fig. 6c,d). Structural comparison showed the spatial conflict of the closed W234 side chain with the acyl part of C14:0-AMP. Indeed, the W234 residue undergoes an orientation rearrangement characterized with the rotation of an indole ring by 55.7° around the C_β–C_γ bond (Fig. 6e). This implies that the conformational reorientation of W234 from the closed state to an open state is a prerequisite for the loading of eFA by ttFACS[49]. Sequence and structure alignments suggested an equivalent residue W230 in AasS. Unlike the apo form of AasS with W230 in the closed conformation (Fig. 6f), both FA substrates (E-pim and oleate; Fig. 6g,h) and the intermediate acyl-adenylates (M-pim-AMP and C18:1-AMP) consistently resulted in the W230 gatekeeper being orientationally rearranged into an almost-identical open state. The W230 residue remains in the closed conformation regardless of whether AasS binds ATP or its analog AMP-PNP (Fig. 6i–l). An open conformation of W230 was observed in AasS complexed with its final products M-pim-ACP and C18:1-ACP (Fig. 6m,n). Similar to that of ttFACS (Fig. 6e), the AasS W230 residue was measured to undergo conformational reorientation (Fig. 6o). This raises the possibility that W230 determines FA loading by AasS machinery.

The difference between ttFACS and AasS is a critical factor that induces the orientational alteration of the gating residue. The binding of ATP is considered as the factor that induces the orientation rearrangement of W234 in ttFACS[49]. However, the W230 residue remains conformationally unchanged in the two complexes of AasS with AMP-PNP (Fig. 6i) and ATP (Fig. 6j). In contrast to that of the ttFACS–AMP-PNP complex, the γ-phosphate of AMP-PNP within AasS adopts an opposite conformation (Supplementary Fig. 28). The structures of the AasS–E-pim and AasS–C18:1 complexes unambiguously showed that W230 undergoes orientation rearrangement upon binding to the FA substrate (Fig. 6g,h). Moreover, W230 appears to pin the FA chain against the tunnel wall in the acyl-bound structures (Fig. 6g–n). This assured an advantage of AasS in stabilizing the FA substrates for catalysis. Lastly, all three mutants (W230A, W230R and W230Y) we generated were found to be greatly ineffective with the E-pim substrate (Fig. 6p) and largely hampered the viability of the Δ*bioC* strain (Fig. 6q,r). In summary, AasS exploits the gating residue W230 to accommodate diverse FA substrates, independent of ATP binding.

Discussion

The flexibility of structural organization accounts for functional differentiation within the AAE family[45,66], in which conformational rearrangement is a prerequisite for AAE catalysis[55,76]. Before this study, it was known that the AAE superfamily comprises a set of structurally diverse members (Supplementary Fig. 29a–c). Structural organization of AAE-type enzymes varies from monomer (such as firefly luciferase[47] and *M. tuberculosis* FadD32 (ref. 78)) to trimer (yeast acetyl-coA synthetase[50]). Supported by increasingly accumulated structures of AAE enzymes (for example, ttFACS[49], FadD10 of *M. tuberculosis*[65] and FmoA3, a nonribosomal peptide synthetase[79]), it seems likely that the dimeric form is the prevalent form of AAE enzymes (Supplementary Fig. 29b). Through cryo-EM study combined with biochemical analysis, we revealed that the versatile AasS enzyme acts as a hexamer (Fig. 1 and Supplementary Fig. 29d), which explains the oligomeric organization of around 330 kDa observed 30 years ago[25]. More importantly, we provide evidence for a previously unclear mechanism through which AasS mediates the activation and recycling of eFA[25,52,62]. We describe the complete catalytic landscape of the versatile AasS enzyme (Fig. 7). In brief, FAs of various length are trapped in a hydrophobic and sticky tunnel, ATP enters a pocket near the tunnel and the two domains (AasS_N and AasS_C) cooperate together during the transfer of AMP to the FA carboxyl group (Fig. 7). After formation of the acyl-AMP intermediate, AasS reverts back to a hexamer and ACP-Ppan enters from an opening in the AasS_N domain, most likely captured by its complementary interaction with the C-terminal domain (Fig. 7 and Extended Data Fig. 7). AasS_C shifts ~154° and adopts the closed conformation. The acyl group is transferred to the Ppan moiety and produces fatty acyl-ACP and AMP. After product release, AasS reverts to its open conformation (Fig. 7).

To the best of current knowledge, most acyl-CoA synthetases (exemplified with ttFACS of *T. hermophilus*[49], CBL[69] and human ACSM2A (ref. 76)) invariantly display two distinct conformations. Analogous

Fig. 6 | Functional dissection of the gating role of W230 in AasS catalysis. **a**, The closed conformation of the gating residue W234 in the apo form of ttFACS. **b**,**c**, The open conformation of the gate residue W234 consistently occurs in ttFACS bound to AMP-PNP (**b**) or C14:0-AMP (**c**). **d**, Structural superposition suggests that the gate residue W234 is conformationally altered upon the binding of AMP-PNP or C14:1-AMP. **e**, Structural superposition of ttFACS suggests the rotation of an indole ring of the W234 residue by 55.7°. **f**, The closed conformation of residue W230 in the apo form of AasS. **g**, The open conformation of residue W230 in AasS with E-pim liganded. **h**, The open conformation of residue W230 in AasS with oleate bound. **i**,**j**, The closed conformation of residue W230 invariantly appears in AasS regardless of AMP-PNP (**i**) or ATP (**j**) being bound. **k**–**n**, The open conformation of W230 is visualized in a panel of AasS complexes with M-pim-AMP (**k**), C18:1-AMP (**l**), M-pim-ACP (**m**) or C18:1-ACP (**n**). **o**, Structural alignments of AasS alone and its complexes show that the W230 gating residue undergoes a rotation of the indole ring by 89.9°. **p**, The impairment in enzymatic activities of the three AasS mutants in vitro. **q**, The single mutant W230A (W230R and/or W230Y) loses the ability of AasS to allow the growth of Δ*bioC* on M9 minimal agar plates with E-pim as the sole carbon source. **r**, Growth curves of the biotin auxotrophic Δ*bioC* strain carrying certain AasS mutants (W230A, W230R or W230Y) in M9 minimal medium with E-pim as the sole carbon source.

https://doi.org/10.1038/s41594-024-01464-7

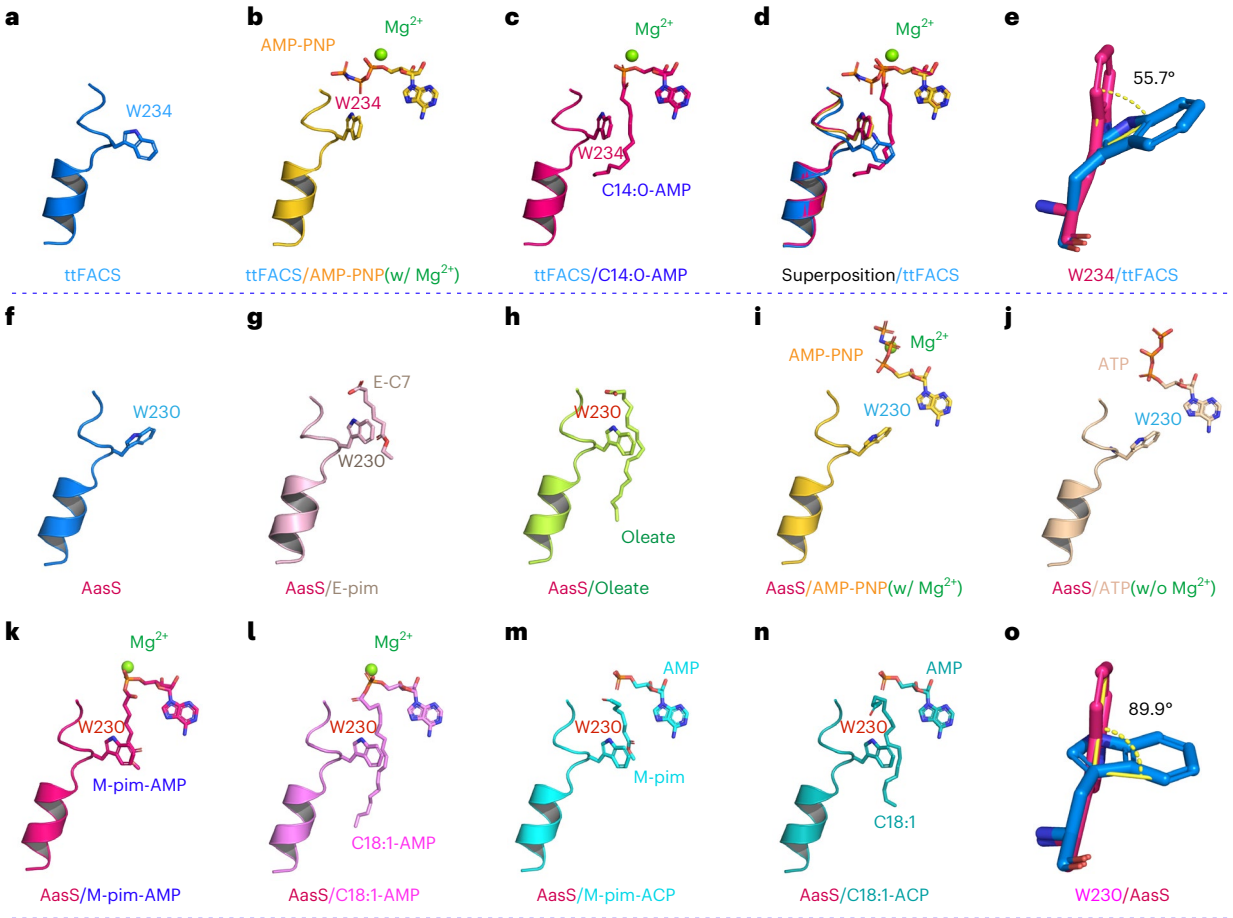

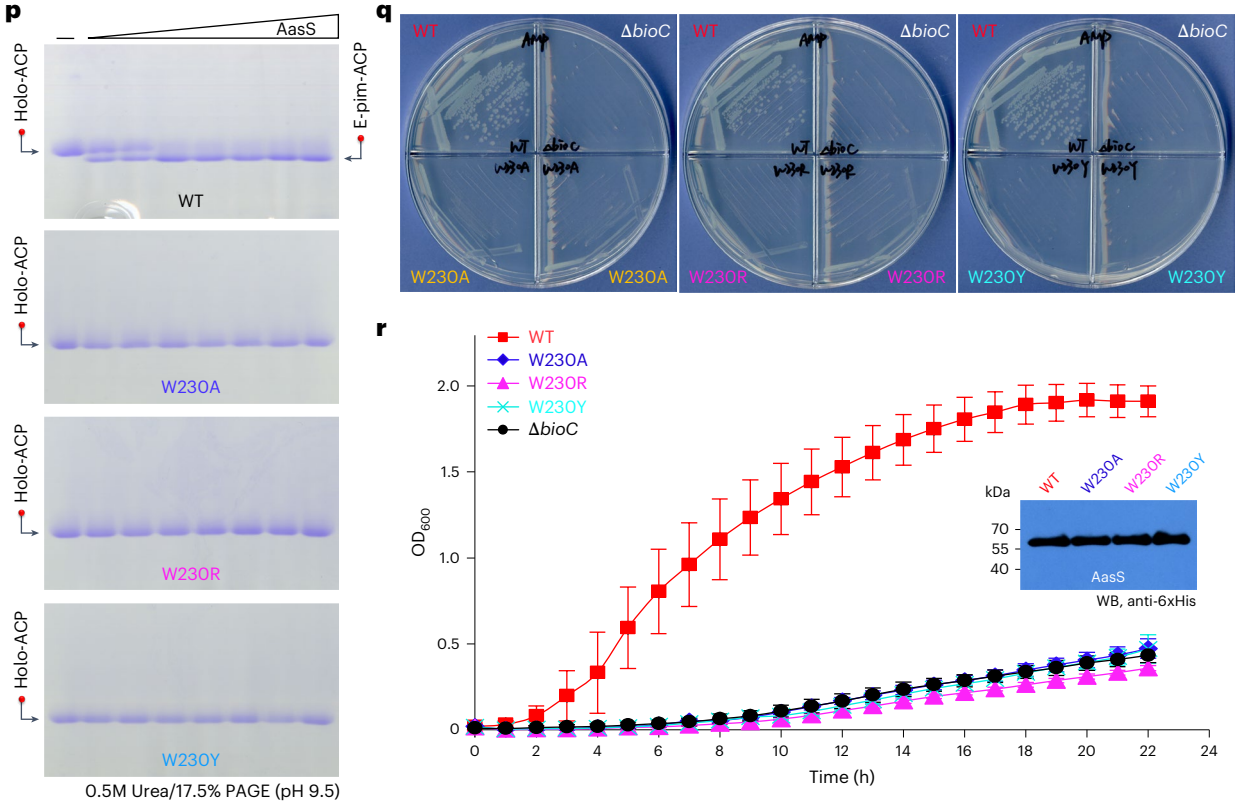

https://doi.org/10.1038/s41594-024-01464-7

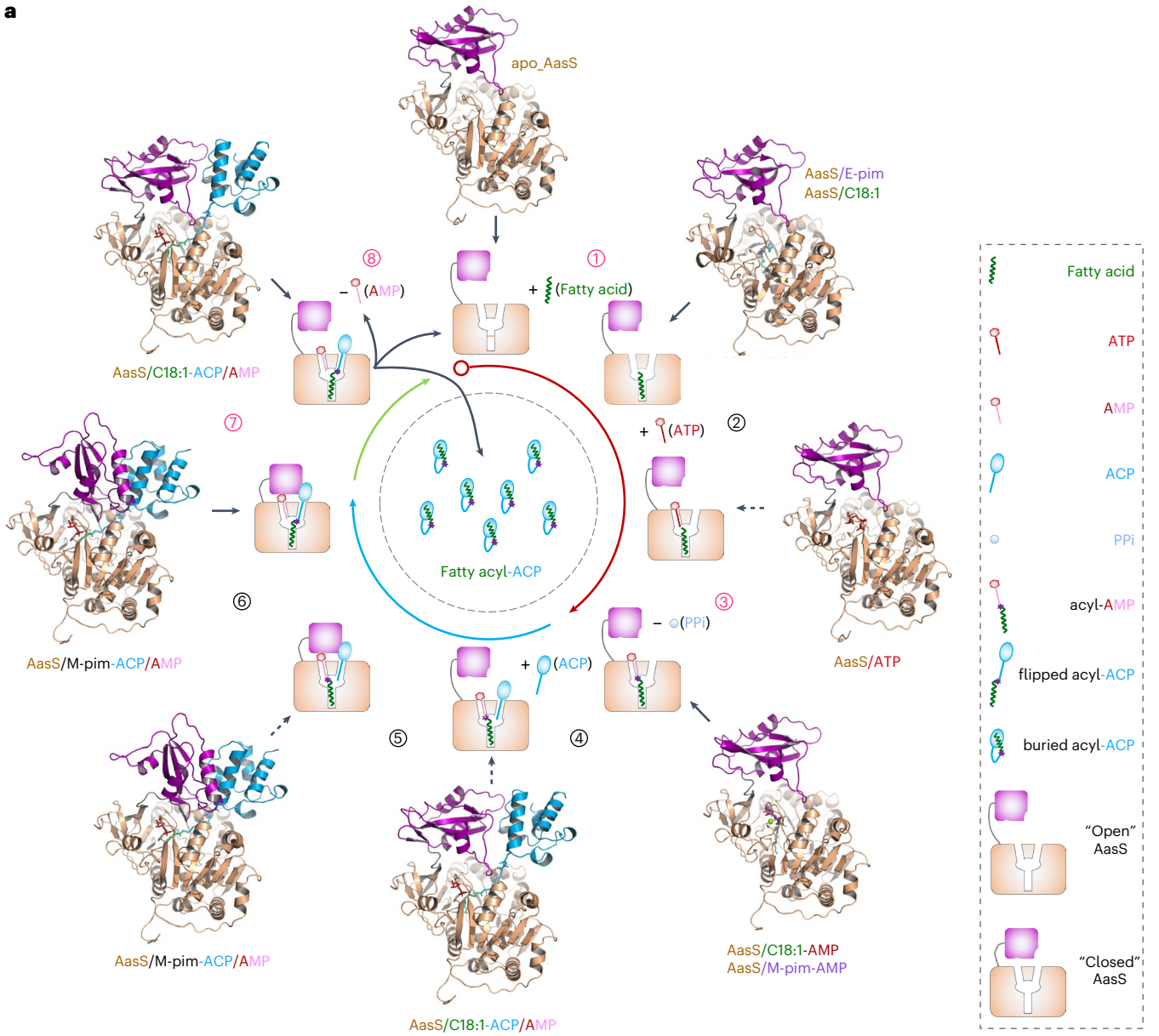

Fig. 7 | A working model explaining how AasS recycles and activates eFA. **a**, Structural landscapes of AasS catalysis engaged in eFA activation and use. Only a protomer of AasS is used here to distinguish its open conformation from the closed conformation. The protomer of AasS contains an N-terminal domain (chocolate yellow) connected by a short loop motif (gray) with a C-terminal domain (purple). During the catalytic cycle, AasS successively binds three different substrates: (i) FAs, (ii) ATP and (iii) the ACP carrier. As for the first committed step of the AasS reaction, the FA substrate (green) firstly opens the gating residue W230 for its entry. After the access of ATP (dark red) to the adenylate-binding site, AasS ligates FAs with ATP to give an acyl-AMP intermediate and release a pyrophosphoric acid. In the second step, the binding of AasS to holo-ACP protein (blue) induces its C-terminal domain movement. The C-terminal domain orientation shift presumably stabilizes the ACP binding. Then, AasS catalyzes the formation of the fatty acyl-ACP and AMP. After the second step, the C-terminal domain is restored to its initial orientation. Finally, AasS releases the end-products fatty acyl-ACP and AMP and reverts to its apo form. Briefly, the AasS catalysis cycle is divided into three stages: (i) an adenylate-forming stage (dark red circular arrow); (ii) the thioester-producing stage (blue circular arrow); and (iii) the recovery stage (light-green circular arrow). The cartoon snapshot of each state presented here is dependent on the cryo-EM structure indicated by a black arrow. A series of AasS structures enabled us to propose the intermediate states of catalysis, which are shown with dashed arrows. All steps are numbered, with critical steps colored red. **b**, A possible route for the AasS tetramer, a putative catalytic intermediate, transformed from its stable hexamer form in the presence of $MgCl_2$ plus ATP or its analog AMP-PNP. A possible step of AasS transformation from a hexamer into a tetramer is indicated by a rectangle with dashed lines.

to these enzymes, the AasS_C domain is capable of adopting both conformations (Fig. 5 and Extended Data Fig. 8). Eight of our nine AasS structures consistently displayed an adenylate-forming conformation, with the only exception referring to AasS–M-pim-ACP featuring the closed conformation. The closure of the AasS_C domain is critical for the Ppan moiety of the ACP carrier to access the active site[14,78]. Indeed, what we captured in the AasS–M-pim-ACP structure is the product complex (Fig. 5a–f). However, another product complex of AasS–C18:1-ACP was in the adenylate-forming open conformation. Because such an open conformation lacks specific interactions between ACP and AasS_C, it seems likely to be a conformational state after product formation and before oleoyl-ACP release. Moreover, the AasS_C domain reverting back to the adenylate-forming apo conformation could be part of the product release mechanism, after which a second catalysis cycle should start (Fig. 7). The hydrophobic pocket in AasS is wider and relatively straight, which in part explains its enzymatic promiscuity[62]. The fatty acyl binding-driven major alteration in AasS lies in the rotation of the W230 residue, which packs against the acyl part of FAs near the carboxyl end. The rotation of the W230 indole ring constitutes an explanation for the flexibility of AasS in the recognition of various FA substrates (Fig. 6 and Extended Data Fig. 6).

The substrate promiscuity of *V. harveyi* AasS provides the basis for its functional versatility[62]. For example, AasS can be used as a tool in synthetic biology for the production of different hydrocarbon species and leveraged to gain access to previously inaccessible metabolic pathways[62,80]. Given that palmitoleic acid (C16:1, Δ9), a host unsaturated FA, was recently found to potentiate gentamycin killing of methicillin-resistant *S. aureus* by perturbing the bacterial membrane and improving antibiotic uptake[81], we believe that the AasS-lacking pathogen *Vibrio cholerae* is accordingly susceptible to combination therapy with palmitoleic acid. Recently, Carfrae et al. showed that FAS II route-directed inhibition efficiently overcomes bacterial polymyxin resistance[16]. Thus, it can be assumed that bypassing the FAS II path through AasS-aided eFA recycling potentially challenges the renewed interest in resensitizing *mcr-1*-positive superbugs with colistin resistance using FAS II-targeted antimicrobials[16].

Online content

Any methods, additional references, Nature Portfolio reporting summaries, source data, extended data, supplementary information, acknowledgements, peer review information; details of author contributions and competing interests; and statements of data and code availability are available at https://doi.org/10.1038/s41594-024-01464-7.

References

1. Radka, C. D. & Rock, C. O. Mining fatty acid biosynthesis for new antimicrobials. *Annu. Rev. Microbiol.* **76**, 281–304 (2022).
2. Parsons, J. B. & Rock, C. O. Bacterial lipids: metabolism and membrane homeostasis. *Prog. Lipid Res.* **52**, 249–276 (2013).
3. Yao, J. & Rock, C. O. How bacterial pathogens eat host lipids: implications for the development of fatty acid synthesis therapeutics. *J. Biol. Chem.* **290**, 5940–5946 (2015).
4. Campbell, J. W. & Cronan, J. E. Jr. Bacterial fatty acid biosynthesis: targets for antibacterial drug discovery. *Annu. Rev. Microbiol.* **55**, 305–332 (2001).
5. Balemans, W. et al. Essentiality of FASII pathway for *Staphylococcus aureus*. *Nature* **463**, E3 (2010).
6. Cronan, J. E. The acyl carrier proteins of lipid synthesis are busy having other affairs. *Biochem. J.* **480**, 855–873 (2023).
7. Leibundgut, M., Jenni, S., Frick, C. & Ban, N. Structural basis for substrate delivery by acyl carrier protein in the yeast fatty acid synthase. *Science* **316**, 288–290 (2007).
8. Nguyen, C. et al. Trapping the dynamic acyl carrier protein in fatty acid biosynthesis. *Nature* **505**, 427–431 (2014).
9. Zhang, L. et al. Crystal structure of FabZ–ACP complex reveals a dynamic seesaw-like catalytic mechanism of dehydratase in fatty acid biosynthesis. *Cell Res.* **26**, 1330–1344 (2016).
10. Bi, H., Zhu, L., Jia, J., Zeng, L. & Cronan, J. E. Unsaturated fatty acid synthesis in the gastric pathogen *Helicobacter pylori* proceeds via a backtracking mechanism. *Cell Chem. Biol.* **23**, 1480–1489 (2016).
11. Zhou, J. et al. *Helicobacter pylori* FabX contains a [4Fe–4S] cluster essential for unsaturated fatty acid synthesis. *Nat. Commun.* **12**, 6932 (2021).
12. Sztain, T. et al. Decoding allosteric regulation by the acyl carrier protein. *Proc. Natl Acad. Sci. USA* **118**, e2025597118 (2021).
13. Cryle, M. J. & Schlichting, I. Structural insights from a P450 carrier protein complex reveal how specificity is achieved in the $P450_{Biol}$ ACP complex. *Proc. Natl Acad. Sci. USA* **105**, 15696–15701 (2008).
14. Agarwal, V., Lin, S., Lukk, T., Nair, S. K. & Cronan, J. E. Structure of the enzyme–acyl carrier protein (ACP) substrate gatekeeper complex required for biotin synthesis. *Proc. Natl Acad. Sci. USA* **109**, 17406–17411 (2012).
15. Cronan, J. E. The chain-flipping mechanism of ACP (acyl carrier protein)-dependent enzymes appears universal. *Biochem. J.* **460**, 157–163 (2014).
16. Carfrae, L. A. et al. Inhibiting fatty acid synthesis overcomes colistin resistance. *Nat. Microbiol.* **8**, 1026–1038 (2023).
17. Yao, J. & Rock, C. O. Exogenous fatty acid metabolism in bacteria. *Biochimie* **141**, 30–39 (2017).
18. Parsons, J. B., Frank, M. W., Subramanian, C., Saenkham, P. & Rock, C. O. Metabolic basis for the differential susceptibility of Gram-positive pathogens to fatty acid synthesis inhibitors. *Proc. Natl Acad. Sci. USA* **108**, 15378–15383 (2011).
19. Brinster, S. et al. Type II fatty acid synthesis is not a suitable antibiotic target for Gram-positive pathogens. *Nature* **458**, 83–86 (2009).
20. Radka, C. D. Interfacial enzymes enable Gram-positive microbes to eat fatty acids. *Membranes* **13**, 423 (2023).

21. Black, P. N., DiRusso, C. C., Metzger, A. K. & Heimert, T. L. Cloning, sequencing, and expression of the *fadD* gene of *Escherichia coli* encoding acyl coenzyme A synthetase. *J. Biol. Chem.* **267**, 25513–25520 (1992).
22. Ray, T. K. & Cronan, J. E. Jr. Activation of long chain fatty acids with acyl carrier protein: demonstration of a new enzyme, acyl-acyl carrier protein synthetase in *Escherichia coli*. *Proc. Natl Acad. Sci. USA* **73**, 4374–4378 (1976).
23. Rock, C. O. & Cronan, J. E. Jr. Acyl-acyl carrier protein synthetase from *Escherichia coli*. *Methods Enzymol.* **71 Pt C**, 163–168 (1981).
24. Rock, C. O. & Cronan, J. E. Jr. Solubilization, purification, and salt activation of acyl-acyl carrier protein synthetase from *Escherichia coli*. *J. Biol. Chem.* **254**, 7116–7122 (1979).
25. Fice, D., Shen, Z. & Byers, D. M. Purification and characterization of fatty acyl-acyl carrier protein synthetase from *Vibrio harveyi*. *J. Bacteriol.* **175**, 1865–1870 (1993).
26. Shen, Z., Fice, D. & Byers, D. M. Preparation of fatty-acylated derivatives of acyl carrier protein using *Vibrio harveyi* acyl-ACP synthetase. *Anal. Biochem.* **204**, 34–39 (1992).
27. Byers, D. M. & Holmes, C. G. A soluble fatty acyl-acyl carrier protein synthetase from the bioluminescent bacterium *Vibrio harveyi*. *Biochem. Cell Biol.* **68**, 1045–1051 (1990).
28. Parsons, J. B. et al. Identification of a two-component fatty acid kinase responsible for host fatty acid incorporation by *Staphylococcus aureus*. *Proc. Natl Acad. Sci. USA* **111**, 10532–10537 (2014).
29. Parsons, J. B., Frank, M. W., Jackson, P., Subramanian, C. & Rock, C. O. Incorporation of extracellular fatty acids by a fatty acid kinase-dependent pathway in *Staphylococcus aureus*. *Mol. Microbiol.* **92**, 234–245 (2014).
30. Subramanian, C., Cuypers, M. G., Radka, C. D., White, S. W. & Rock, C. O. Domain architecture and catalysis of the *Staphylococcus aureus* fatty acid kinase. *J. Biol. Chem.* **298**, 101993 (2022).
31. Shi, Y. et al. Structure and mechanism for streptococcal fatty acid kinase (Fak) system dedicated to host fatty acid scavenging. *Sci. Adv.* **8**, eabq3944 (2022).
32. Gullett, J. M., Cuypers, M. G., Frank, M. W., White, S. W. & Rock, C. O. A fatty acid-binding protein of *Streptococcus pneumoniae* facilitates the acquisition of host polyunsaturated fatty acids. *J. Biol. Chem.* **294**, 16416–16428 (2019).
33. Cuypers, M. G. et al. Acyl-chain selectivity and physiological roles of *Staphylococcus aureus* fatty acid-binding proteins. *J. Biol. Chem.* **294**, 38–49 (2019).
34. Broussard, T. C. et al. Biochemical roles for conserved residues in the bacterial fatty acid-binding protein family. *J. Biol. Chem.* **291**, 6292–6303 (2016).
35. Coleman, J. Characterization of the *Escherichia coli* gene for 1-acyl-*sn*-glycerol-3-phosphate acyltransferase (*plsC*). *Mol. Gen. Genet.* **232**, 295–303 (1992).
36. Lightner, V. A. et al. Membrane phospholipid synthesis in *Escherichia coli*. Cloning of a structural gene (*plsB*) of the *sn*-glycerol-3-phosphate acyl/transferase. *J. Biol. Chem.* **255**, 9413–9420 (1980).
37. Larson, T. J., Lightner, V. A., Green, P. R., Modrich, P. & Bell, R. M. Membrane phospholipid synthesis in *Escherichia coli*. Identification of the *sn*-glycerol-3-phosphate acyltransferase polypeptide as the *plsB* gene product. *J. Biol. Chem.* **255**, 9421–9426 (1980).
38. Yao, J., Bruhn, D. F., Frank, M. W., Lee, R. E. & Rock, C. O. Activation of exogenous fatty acids to acyl-acyl carrier protein cannot bypass FabI inhibition in *Neisseria*. *J. Biol. Chem.* **291**, 171–181 (2016).
39. Lu, Y. J. et al. Acyl-phosphates initiate membrane phospholipid synthesis in Gram-positive pathogens. *Mol. Cell* **23**, 765–772 (2006).
40. DeMars, Z., Singh, V. K. & Bose, J. L. Exogenous fatty acids remodel *Staphylococcus aureus* lipid composition through fatty acid kinase. *J. Bacteriol.* **202**, e00128-20 (2020).
41. DeMars, Z. & Bose, J. L. Redirection of metabolism in response to fatty acid kinase in *Staphylococcus aureus*. *J. Bacteriol.* **200**, e00345-18 (2018).
42. Teoh, W. P., Chen, X., Laczkovich, I. & Alonzo, F. 3rd *Staphylococcus aureus* adapts to the host nutritional landscape to overcome tissue-specific branched-chain fatty acid requirement. *Proc. Natl Acad. Sci. USA* **118**, e2022720118 (2021).
43. Frank, M. W. et al. Host fatty acid utilization by *Staphylococcus aureus* at the infection site. *mBio* **11**, e00920-20 (2020).
44. Morvan, C. et al. Environmental fatty acids enable emergence of infectious *Staphylococcus aureus* resistant to FASII-targeted antimicrobials. *Nat. Commun.* **7**, 12944 (2016).
45. Schmelz, S. & Naismith, J. H. Adenylate-forming enzymes. *Curr. Opin. Struct. Biol.* **19**, 666–671 (2009).
46. Sundlov, J. A., Fontaine, D. M., Southworth, T. L., Branchini, B. R. & Gulick, A. M. Crystal structure of firefly luciferase in a second catalytic conformation supports a domain alternation mechanism. *Biochemistry* **51**, 6493–6495 (2012).
47. Conti, E., Franks, N. P. & Brick, P. Crystal structure of firefly luciferase throws light on a superfamily of adenylate-forming enzymes. *Structure* **4**, 287–298 (1996).
48. Baldwin, T. O. Firefly luciferase: the structure is known, but the mystery remains. *Structure* **4**, 223–228 (1996).
49. Hisanaga, Y. et al. Structural basis of the substrate-specific two-step catalysis of long chain fatty acyl-CoA synthetase dimer. *J. Biol. Chem.* **279**, 31717–31726 (2004).
50. Jogl, G. & Tong, L. Crystal structure of yeast acetyl-coenzyme A synthetase in complex with AMP. *Biochemistry* **43**, 1425–1431 (2004).
51. Gulick, A. M., Lu, X. & Dunaway-Mariano, D. Crystal structure of 4-chlorobenzoate:CoA ligase/synthetase in the unliganded and aryl substrate-bound states. *Biochemistry* **43**, 8670–8679 (2004).
52. Jiang, Y., Chan, C. H. & Cronan, J. E. The soluble acyl-acyl carrier protein synthetase of *Vibrio harveyi* B392 is a member of the medium chain acyl-CoA synthetase family. *Biochemistry* **45**, 10008–10019 (2006).
53. Tanovic, A., Samel, S. A., Essen, L. O. & Marahiel, M. A. Crystal structure of the termination module of a nonribosomal peptide synthetase. *Science* **321**, 659–663 (2008).
54. May, J. J., Kessler, N., Marahiel, M. A. & Stubbs, M. T. Crystal structure of DhbE, an archetype for aryl acid activating domains of modular nonribosomal peptide synthetases. *Proc. Natl Acad. Sci. USA* **99**, 12120–12125 (2002).
55. Gulick, A. M. Conformational dynamics in the acyl-CoA synthetases, adenylation domains of non-ribosomal peptide synthetases, and firefly luciferase. *ACS Chem. Biol.* **4**, 811–827 (2009).
56. Cusack, S., Yaremchuk, A. & Tukalo, M. The crystal structure of the ternary complex of *T. thermophilus* seryl-tRNA synthetase with $tRNA^{Ser}$ and a seryl-adenylate analogue reveals a conformational switch in the active site. *EMBO J.* **15**, 2834–2842 (1996).
57. Cusack, S., Berthet-Colominas, C., Hartlein, M., Nassar, N. & Leberman, R. A second class of synthetase structure revealed by X-ray analysis of *Escherichia coli* seryl-tRNA synthetase at 2.5 Å. *Nature* **347**, 249–255 (1990).
58. Biou, V., Yaremchuk, A., Tukalo, M. & Cusack, S. The 2.9 Å crystal structure of *T. thermophilus* seryl-tRNA synthetase complexed with $tRNA^{Ser}$. *Science* **263**, 1404–1410 (1994).
59. Bilokapic, S. et al. Structure of the unusual seryl-tRNA synthetase reveals a distinct zinc-dependent mode of substrate recognition. *EMBO J.* **25**, 2498–2509 (2006).

60. Schmelz, S. et al. AcsD catalyzes enantioselective citrate desymmetrization in siderophore biosynthesis. *Nat. Chem. Biol.* **5**, 174–182 (2009).
61. Duckworth, B. P., Nelson, K. M. & Aldrich, C. C. Adenylating enzymes in *Mycobacterium tuberculosis* as drug targets. *Curr. Top. Med. Chem.* **12**, 766–796 (2012).
62. Beld, J., Finzel, K. & Burkart, M. D. Versatility of acyl-acyl carrier protein synthetases. *Chem. Biol.* **21**, 1293–1299 (2014).
63. Trivedi, O. A. et al. Enzymic activation and transfer of fatty acids as acyl-adenylates in mycobacteria. *Nature* **428**, 441–445 (2004).
64. Arora, P. et al. Mechanistic and functional insights into fatty acid activation in *Mycobacterium tuberculosis*. *Nat. Chem. Biol.* **5**, 166–173 (2009).
65. Liu, Z., Ioerger, T. R., Wang, F. & Sacchettini, J. C. Structures of *Mycobacterium tuberculosis* FadD10 protein reveal a new type of adenylate-forming enzyme. *J. Biol. Chem.* **288**, 18473–18483 (2013).
66. Goyal, A., Verma, P., Anandhakrishnan, M., Gokhale, R. S. & Sankaranarayanan, R. Molecular basis of the functional divergence of fatty acyl-AMP ligase biosynthetic enzymes of *Mycobacterium tuberculosis*. *J. Mol. Biol.* **416**, 221–238 (2012).
67. Jiang, Y., Morgan-Kiss, R. M., Campbell, J. W., Chan, C. H. & Cronan, J. E. Expression of *Vibrio harveyi* acyl-ACP synthetase allows efficient entry of exogenous fatty acids into the *Escherichia coli* fatty acid and lipid A synthetic pathways. *Biochemistry* **49**, 718–726 (2010).
68. Burgi, J. et al. Asymmetric horseshoe-like assembly of peroxisomal yeast oxalyl-CoA synthetase. *Biol. Chem.* **404**, 195–207 (2023).
69. Reger, A. S., Wu, R., Dunaway-Mariano, D. & Gulick, A. M. Structural characterization of a 140° domain movement in the two-step reaction catalyzed by 4-chlorobenzoate:CoA ligase. *Biochemistry* **47**, 8016–8025 (2008).
70. Lin, S., Hanson, R. E. & Cronan, J. E. Biotin synthesis begins by hijacking the fatty acid synthetic pathway. *Nat. Chem. Biol.* **6**, 682–688 (2010).
71. Andreini, C., Bertini, I., Cavallaro, G., Holliday, G. L. & Thornton, J. M. Metal ions in biological catalysis: from enzyme databases to general principles. *J. Biol. Inorg. Chem.* **13**, 1205–1218 (2008).
72. Yamagami, R., Huang, R. & Bevilacqua, P. C. Cellular concentrations of nucleotide diphosphate-chelated magnesium ions accelerate catalysis by RNA and DNA enzymes. *Biochemistry* **58**, 3971–3979 (2019).
73. Ahdash, Z. et al. Mechanistic insight into the assembly of the HerA–NurA helicase–nuclease DNA end resection complex. *Nucleic Acids Res.* **45**, 12025–12038 (2017).
74. Yao, J., Dodson, V. J., Frank, M. W. & Rock, C. O. *Chlamydia trachomatis* scavenges host fatty acids for phospholipid synthesis via an acyl-acyl carrier protein synthetase. *J. Biol. Chem.* **290**, 22163–22173 (2015).
75. Radka, C. D., Frank, M. W., Rock, C. O. & Yao, J. Fatty acid activation and utilization by *Alistipes finegoldii*, a representative Bacteroidetes resident of the human gut microbiome. *Mol. Microbiol.* **113**, 807–825 (2020).
76. Kochan, G., Pilka, E. S., von Delft, F., Oppermann, U. & Yue, W. W. Structural snapshots for the conformation-dependent catalysis by human medium-chain acyl-coenzyme A synthetase ACSM2A. *J. Mol. Biol.* **388**, 997–1008 (2009).
77. Zhang, Z. et al. Structural and functional studies of fatty acyl adenylate ligases from *E. coli* and *L. pneumophila*. *J. Mol. Biol.* **406**, 313–324 (2011).
78. Kuhn, M. L. et al. Structure of the essential Mtb FadD32 enzyme: a promising drug target for treating tuberculosis. *ACS Infect. Dis.* **2**, 579–591 (2016).
79. Katsuyama, Y. et al. Structural and functional analyses of the tridomain-nonribosomal peptide synthetase FmoA3 for 4-methyloxazoline ring formation. *Angew. Chem. Int. Ed.* **60**, 14554–14562 (2021).
80. Campopiano, D. J. ACP—AasS you like it. *Chem. Biol.* **21**, 1257–1259 (2014).
81. Papadopoulou, V. et al. Overcoming biological barriers to improve treatment of a *Staphylococcus aureus* wound infection. *Cell Chem. Biol.* **30**, 513–526 (2023).
82. Feng, Y. et al. A *Francisella* virulence factor catalyses an essential reaction of biotin synthesis. *Mol. Microbiol.* **91**, 300–314 (2014).

Publisher's note Springer Nature remains neutral with regard to jurisdictional claims in published maps and institutional affiliations.

Open Access This article is licensed under a Creative Commons Attribution-NonCommercial-NoDerivatives 4.0 International License, which permits any non-commercial use, sharing, distribution and reproduction in any medium or format, as long as you give appropriate credit to the original author(s) and the source, provide a link to the Creative Commons licence, and indicate if you modified the licensed material. You do not have permission under this licence to share adapted material derived from this article or parts of it. The images or other third party material in this article are included in the article's Creative Commons licence, unless indicated otherwise in a credit line to the material. If material is not included in the article's Creative Commons licence and your intended use is not permitted by statutory regulation or exceeds the permitted use, you will need to obtain permission directly from the copyright holder. To view a copy of this licence, visit http://creativecommons.org/licenses/by-nc-nd/4.0/.

© The Author(s) 2025

[1]Key Laboratory of Multiple Organ Failure (Ministry of Education), Departments of Microbiology and General Intensive Care Unit of the Second Affiliated Hospital, Zhejiang University School of Medicine, Hangzhou, China. [2]Department of Biophysics and Department of Pathology of Sir Run Run Shaw Hospital, Zhejiang University School of Medicine, Hangzhou, China. [3]School of Life Sciences, Northwestern Polytechnical University, Xi'an, China. [4]Cancer Center at Illinois, University of Illinois at Urbana-Champaign, Urbana, IL, USA. [5]School of Public Health, Zhejiang University School of Medicine, Hangzhou, China. [6]Center of Cryo-Electron Microscopy, Zhejiang University, Hangzhou, China. [7]Department of Clinical Laboratory, Shenzhen Third People's Hospital, National Clinical Research Center for Infectious Diseases, The Second Affiliated Hospital of Southern University of Science and Technology, Shenzhen, China. [8]These authors contributed equally: Haomin Huang, Chen Wang, Shenghai Chang, Tao Cui. ✉e-mail: chunzhou@zju.edu.cn; xzhang1999@zju.edu.cn; fengyj@zju.edu.cn

Methods

Strains, plasmids, primers and growth conditions

All the bacterial strains used here were derivatives of *E. coli* MG1655 (Supplementary Table 2). DH5α was used for gene cloning and BL21(DE3) was applied in protein overexpression. Strain FYJ582, BL21(DE3) bearing the recombinant plasmid pET28a::*aasS*, was subjected to the production of AasS enzyme. The biotin auxotroph strain (Δ*bioC*), called STL96 (ref. 83), functioned as an indicator host to verify altered abilities of AasS and its derivatives in bypassing the initial BioC step of biotin synthesis. In this case, we created a constitutive expression vector, designated as pET21a-P*rmpA*, in which the former T7 strong promoter is replaced with the modest promoter (P*rmpA*) of *Klebsiella pneumoniae* virulence regulator *rmpA*[84,85], in front of multiple cloning sites, on the basis of a pET21a backbone (Supplementary Table 2). The *aasS* gene was introduced into pET21a-P*rmpA*, giving a recombinant version of pET21a-P*rmpA::aasS* dedicated to subsequent functional assays (Supplementary Table 2). Accordingly, the two *aasS*-harboring expression plasmids (pET28a::*aasS* plus pET21a-P*rmpA::aasS*) acted as templates to generate a series of AasS mutants, using the approach of structure-guided and site-directed mutagenesis. In total, 66 AasS mutants (33 per vector) were generated, which were exemplified with the substituted W230 gating residue, including but not limited to (1) FYJ6014 (STL96 containing pET21a-P*rmpA::aasS*(W230A)) and (2) FYJ6047 (BL21(DE3) carrying pET28a::*aasS*(W230A)). To examine the role of the AasS_C domain, a deletion mutant of AasS devoid of AasS_C, named AasS(ΔC), was engineered, producing FYJ6017 (Δ*bioC*/pET21a-P*rmpA::aasS*(ΔC)) and FYJ6050 (BL21(DE3)/pET28a::*aasS*(ΔC)). In addition to routine PCR detection with specific primers (Supplementary Table 3), all resultant plasmids were determined by Sanger DNA sequencing. The *E. coli* Δ*bioC* strains we developed were routinely maintained on Luria–Bertani (LB) broth or assayed for AasS activity in the biotin-lacking M9 minimal medium. When necessary, antibiotics were supplemented with 100 μg ml^{-1} ampicillin and 50 μg ml^{-1} kanamycin.

Protein expression, purification and identification

The recombinant form of AasS enzyme was prepared from a 1-L culture of strain FYJ582 induced with 0.3 mM IPTG at 16 °C overnight. The cell pellets obtained by centrifugation were washed and lysed in lysis buffer (50 mM Tris-HCl pH 8.0, 150 mM NaCl, 5 mM β-mercaptoethanol and 1 mM PMSF). As recently described by Zhang and coworkers with minor changes[86], the clarified supernatants were loaded on Ni-NTA agarose (Qiagen, R90110) to capture the N-terminal 6xHis-tagged AasS protein. Following removal of contaminated proteins with wash buffer containing 20 mM imidazole, the protein of interest was completely eluted with the elution buffer of 300 mM imidazole. Then, it was exchanged with GF buffer (25 mM Tris-HCl pH 8.0, 150 mM NaCl and 2 mM DTT) and concentrated to the level of ~15 mg ml^{-1} before separation by SEC (AKTA Pure) on a Superdex 200 Increase 10/300 column (GE HealthCare). The AasS sample was collected from the target peak and its purity was validated by SDS–PAGE (12%). AasS is eluted as a hexamer. In fact, all the remaining 32 AasS mutants were prepared almost identically to the wild type. All fresh samples of AasS and its derivatives were subjected to cryo-EM study and enzymatic assays in vitro.

To establish the enzymatic reaction of AasS in vitro, we prepared the fatty acyl recipient protein, the *E. coli* holo-ACP, as conducted by Flugel and colleagues[87] with little modification. In brief, strain DK574 (that is, FYJ540 in our lab stock) that carries three plasmids (pMS421 containing the *lacI*^{q} mutation, pMR19421 with a P*tac*-induced *acpP* and pJT93 producing *acpS* under *tac* promoter) was grown in LB medium containing 50 μg ml^{-1} kanamycin, 50 μg ml^{-1} spectinomycin and 10 μg ml^{-1} chloramphenicol)[87]. The bacterial culture (~1 L) with an optical density at 600 nm (OD_{600}) of ~0.8 was chilled with ice and induced overnight with 0.1 mM IPTG at 16 °C. Next, bacterial pellets were resuspended in lysis buffer (50 mM Tris-HCl pH 8.0, 150 mM NaCl, 10 mM $MgSO_4$ and 1 mM DTT) and subjected to lysis by a French press (JN-Mini). The clarified lysates we acquired were incubated with 1 mM CoA trilithium salt at 37 °C for 3 h, mixed with isopropanol (1:1), centrifuged (33,900*g*, 30 min) and then dialyzed in dialysis buffer (50 mM MES potassium salt pH 6.1 and 150 mM NaCl) at 4 °C overnight. Finally, the dialysis products were concentrated and then purified with a HiTrap capto Q column (GE HealthCare). The holo-ACP specie was distinguished from its apo form by the separation with a conformationally sensitive gel using 0.5 M urea and 17.5% PAGE (pH 9.5) as recently described with activities of *Pseudomonas* BioH[88] and three mycobacterial BioH isoforms[89].

AUC analysis

To further confirm the solution state of AasS as a hexamer, an AUC experiment was conducted as earlier reported with BioQ[90]. In brief, AasS enzyme of over 95% purity was diluted to 0.8 mg ml^{-1} in AUC buffer (25 mM Tris-HCl pH 8.0 and 150 mM NaCl). The AasS sample was centrifuged using an Optima AUC-A/I (Beckman Coulter) set at 129,000*g* and 20 °C. Here, a tube of AUC buffer served as the negative control. Data analysis was carried out using 50–100 scans with a continuous c(s) distribution model in SEDFIT software[91], where a peak profile was an indicative of AasS molecular weight (~380 kDa).

Assays for AasS activity in vitro

As earlier described by Jiang and coauthors[52,67], we also established a reaction system of AasS catalysis. In this reaction buffer composed of 100 mM Tris-HCl pH 7.5, 10 mM $MgSO_4$, 5 mM DTT and 10 mM ATP, two substrates (FAs (~0.6 mM) and holo-ACP (~ 75 μg ml^{-1})) were added in the presence of AasS enzyme at different levels (0, 0.15, 0.3, 0.6, 1.5, 3.0, 4.5 and 6.0 nM). Although M-pim, a cognate substrate of BioH, cannot be commercially purchased, it was functionally replaced by the commercially available E-pim in our assays[89]. Thus, E-pim was extensively used as a surrogate substrate to finely dissect altered activities of AasS mutants. In addition to M-pim and E-pim, ten different FAs were included to test the promiscuity of AasS[52,62], namely butyric acid (C4:0), hexanoic acid (C6:0), octanoic acid (C8:0), decanoic acid (C10:0), methyl-glutaric acid (M-C5), myristic acid (C14:0), palmitic acid (C16:0), stearic acid (C18:0), oleic acid (C18:1, Δ9) and linoleic acid (C18:2, Δ9/12). In general, the reaction mixture was kept at 37 °C for 1 h and the resultant acyl-ACP products were detected using a conformationally sensitive 17.5% PAGE gel (pH 9.5) containing 0.5 M urea. Using the software ImageJ, grayscale analyses were performed to relatively quantify the acyl-ACP produced from the reaction catalyzed by AasS and its mutants.

Liquid chromatography with tandem mass spectrometry (LC–MS/MS) identification of acyl-ACP

LC–MS/MS was adopted to accurately map the post-translational modifications of ACP with FAs of varied acyl chain lengths. As recently performed with BioZ and BioH actions[86,89], three kinds of acyl-ACP species (M-pim-ACP, E-pim-ACP and C18:1-ACP) from AasS reactions were cut from the urea gel and digested with pepsin rather than trypsin, giving a collection of peptide mixtures. They were loaded into the trap column (Thermo Fisher Scientific Easy-nLC 1000) before entry into an analytical column (50 μm × 15 cm, nanoViper, C18, 2 μM,100 Å). Coupled with the Thermo LTQ-Orbitrap Elite Ion Trap analyzer (Thermo Fisher Scientific), a Fourier-transform ion cyclotron resonance mass analyzer enabled data collection. Using Proteome Discoverer 2.0, a number of MS spectra were detected, which presumably matched certain acylated ACP peptides with a reliable score. It was noted that many B and Y ion pairs can be generated upon peptide cleavage. In general, 'B' denotes a peptide ion retaining charge at the N terminus and 'Y' refers to a fragment whose charge is retained at the C terminus. As for the mass spectrum, subscript B or Y represents the order of residues in the peptide fragment. The acyl-modified serine residue of interest

was determined by comparing the calculated mass with its theoretical mass within one error value.

Assays for bypass of AasS in biotin synthesis

The principle of examining AasS function relied on two criteria: (1) the *E. coli* Δ*bioC* mutant is a biotin auxotroph, which cannot appear in non-permissive conditions without supplementation of exogenous biotin, and (2) AasS channels exogenous M(E)-pim FAs to holo-ACP and generates M(E)-pim-ACP, a cognate biotin precursor, bypassing the genetic requirement of the primary BioC step[70]. In total, 32 AasS mutants carried by the constitutive vector pET21a-P*rmpA* were assayed for their abilities to confer varied viability of the Δ*bioC* reporter strains on M9 minimal medium lacking biotin. In addition to routine streaking on M9 agar plates, growth curves were plotted for 22 h using a spectrometer (SPECTROstar Nano). Wild-type AasS was used as a positive control. Before data interpretation, all individual colonies bearing *aasS* or its derivatives were determined using western blot with a mouse anti-6x His primary antibody to the C-terminal 6xHis-fused AasS mutants. The primary anti-6x His TAG monoclonal antibody (HIS.H8) was used at a dilution of 1:8,000, while the secondary antibody, horseradish peroxidase-conjugated Affini Pure goat anti-mouse IgG (H + L), was used at a dilution of 1:5,000. On the basis of the cell-free Δ*bioC* crude extract[92], the presence of AasS was also found to allow the in vitro reconstituted system of DTB and biotin synthesis, which is similar to BioH (and its isoform BioJ[82,93])[70,88,89].

ITC-based measurement

To capture the transient interplay between AasS enzyme and its two substrates (E-pim FA and the acyl recipient holo-ACP), ITC experiments were routinely conducted with a microcalorimeter (MicroCal PEAQ-ITC). As previously described with the *E. coli* FadR[94] with little improvement, a total of 19 titrations with an internal time of 150 s were carried out in the volume of 2 µl at 25 °C. The pioneering trials informed us that the E-pim substrate could not be detected to bind AasS alone in our ITC systems without the addition of ATP cofactor. Therefore, before E-pim titration, AasS enzyme (40 µM) was saturated with its ATP cofactor (120 µM) in the cell. The level of E-pim was 600 µM in the syringe. The titration buffer consisted of 150 mM NaCl, 25 mM Tris-HCl pH 8.0, 2 mM DTT and 3 mM $MgCl_2$. Similarly, the holo-ACP (400 µM) in the syringe was titrated against AasS enzyme (40 µM) in the cell. The stoichiometry (n) and dissociation constant (K_d) were measured on the basis of the plotted titration data using a model for one set of sites provided by the MicroCal PEAQ-ITC software. As a result, the final output was presented as the average ±s.d. from three independent experiments[86].

Negative-staining analysis

In addition to AasS alone, eight AasS complexes were prepared for the analyses of negative staining: (1) two cofactor-bound AasS complexes (ATP and AMP-PNP); (2) two FA-liganded AasS complexes (E-pim and C18:1); (3) two AasS-bound adenylate intermediates (M-pim-AMP and C18:1-AMP); and (4) two AasS complexes with final products (M-pim-ACP and C18:1-ACP). The protein samples were separately loaded onto a glow-discharged carbon grid (200 mesh) and stained with 2% uranyl acetate (Acmec, U25690). The prepared grids were routinely examined using a transmission EM instrument operated at 120 kV (Tecnai G2 Spirit, Thermo Fisher Scientific), and then qualified AasS samples were subjected to further quantification and classification analysis.

Cryo-EM sample preparation and data collection

In total, 9 cryo-EM samples were prepared here. As for apo-AasS, an aliquot of 3.0 µl AasS (~20 mg ml^{-1}) mixed with 2 mM Fos-choline 8 was applied to a glow-discharged holey carbon grid (Quantifoil R1.2/1.3, Au, 300 mesh). After a 15-s interval, the grid was blotted for 3.5 s at a humidity of 100% and 22 °C and then plunge-frozen in liquid ethane with a Vitrobot (Thermo Fisher Scientific). It was noted that the reconstitution of different AasS complexes varied dramatically. To generate the ATP-liganded complex, AasS (~0.3 mM) was incubated with 1.5 mM ATP for 30 min at 25 °C before cryo-EM sample production. The other cofactor complex with AMP-PNP, a nonhydrolyzable ATP analog, was obtained through the incubation of 0.35 mM AasS with 5 mM AMP-PNP and 2 mM $MgCl_2$ for 15 min at 25 °C. Unlike the substrate E-pim complex that was generated by mixing 0.154 mM AasS protein with ~300 mM E-pim, the oleate complex was prepared through a 2-h incubation of 0.3 mM AasS with ~1.5 mM oleate at 4 °C. The two adenylate complexes were acquired by incubating 0.25 mM AasS protein with ~0.6 mM M-pim-AMP (and/or ~0.3 mM oleoyl-AMP) for 2 h at 4 °C. Similarly, the two final product-occupied complexes were produced from 0.3 mM AasS protein incubated with ~0.75 mM M-pim-ACP (and/or ~0.2 mM oleoyl-ACP) for 30 min at 25 °C.

Except for the E-pim-bound AasS complex, the eight other cryo-EM samples were imaged using a Titan Krios EM instrument (Thermo Fisher Scientific) operated at 300 kV and equipped with a K2 Summit electron counting direct detection camera (Gatan). Before automated data acquisition by Serial EM software[95], the microscope was adjusted accordingly, especially the coma-free alignment to minimize beam tilt. All cryo-EM images were obtained in counting mode at a nominal magnification of ×29,000, equivalent to a calibrated physical pixel size of 1.014 Å. Defocus was set between −1.5 and −2.5 µm. Each image was recorded at an exposure time of 10 s and dose-fractionated into 40 frames with a dose rate of ~8 counts per second per pixel.

The cryo-EM sample of E-pim-liganded AasS was imaged using a Titan Krios EM instrument coupled with a Falcon4 detector operating at 241 frames per second and a Selectris energy filter. The data were automatically collected with EPU software[96] in place of Serial EM software[95]. All cryo-EM images were obtained at a nominal magnification of ×130,000 (corresponding to a calibrated physical pixel size of 0.93 Å). A total dose of 52 e^- per $Å^2$ with 6-s exposure time was fractionated into 1,442 frames, resulting in a total of 5,381 videos. The defocus parameter was set between −0.6 and −1.5 µm.

Cryo-EM image processing

The beam-induced motion correction of image stacks was carried out using MotionCor[97], generating a series of average micrographs. The contrast transfer function (CTF) parameters of these micrographs were determined with a graphics-processing-unit-accelerated computer program for accurate estimation of the CTF, termed Gctf[98]. Data processing and optimization proceeded using cryoSPARC[99]. For the apo-AasS structure, 454,799 of 772,681 particles were selected for 2D classification and then 213,572 particles were used for three-dimensional (3D) refinement. The reported map with 2.68-Å resolution was given after postprocessing with a B factor of −114 $Å^2$. *D3* symmetry was applied at this step of processing. The overall resolutions were calculated on the basis of the gold-standard Fourier shell correlation (FSC) = 0.143 criterion. Unlike the ATP-liganded AasS complex whose 3D refinement relied on 419,290 of 1,768,321 particles, the analog AMP-PNP complex (appearing as a tetramer rather than a hexamer) was dependent on 282,818 of 1,065,909 particles for *D2* symmetry analysis and 3D classification. As a result, the ATP complex cryo-EM was refined to global resolution of 2.41 Å at an FSC of 0.143, whereas the AMP-PNP complex structure resolution was determined at 2.68 Å with a B factor of −77 $Å^2$. Similarly, 510,518 of 2,109,216 particles were automatically picked for 3D refinement of E-pim substrate-bound AasS complex, producing a map of a 2.15-Å resolution with a B factor of −84 $Å^2$. For the other substrate C18:1-complexed AasS, 217,323 of 968,887 particles were subjected to 3D refinement. This yielded a map at an overall resolution of 2.75 Å with a B factor of −92 $Å^2$. The two adenylate complexes referred to the M-pim-AMP form at 2.76 Å with a B factor of −114 $Å^2$, for which 3D refinement was based on 199,919 of 905,237 particles, and the C18:1-AMP

pattern at 2.59 Å with a *B* factor of −113 Å^2, whose 3D refinement exclusively arose from 397,987 of 799,666 particle projections. Additionally, two final product complexes included the M-pim-ACP-bound type at 2.51 Å with a *B* factor of −85 Å^2, for which 247,748 of 2,481,529 particles allowed the 3D refinement, and the C18:1-ACP-occupied form at 2.63 Å with a *B* factor of −108 Å^2, whose 3D refinement proceeded on 299,233 of 1,540,255 particle projections. Detailed statistics on cryo-EM data processing are available in Table 1.

Model building and refinement

The cryo-EM map of AasS at 2.68 Å enabled us to build its initial model using PHENIX[100]. The crystal structure of the long-chain fatty acyl-CoA synthetase dimer from *T. thermophilus*, abbreviated as ttFACS (Protein Data Bank (PDB) 1V25)[49], was superimposed onto the initial model to produce the entire AasS model in Coot[101]. Following side-chain assignments, the entire AasS structure was manually adjusted and finely refined with phenix.real_space_refine. Then, the apo-AasS structure we obtained acted as a starting model for solving a series of AasS complexes with six ligands: ATP (2.45 Å), AMP-PNP (2.68 Å), E-pim (2.17 Å), C18:1 (2.79 Å), M-pim-AMP (2.77 Å) and oleoyl-AMP (2.61 Å). The densities of relevant ligands were detected from individual cryo-EM maps. Among them, three sets of structural maps were consistently detected to contain a magnesium ion. Accordingly, both ligands and Mg^{2+} were manually fitted in Coot[101], which was followed by the refinement with phenix.real_space_refine. As for the two final product complexes (AasS–M-pim-ACP and AasS–C18:1-ACP), the model of acyl-ACP moieties was built according to a crystal structure of FabZ complexed with holo-ACP (PDB 4ZJB)[9], for which the local density map was manually fitted using UCSF Chimera[102]. The overall complex models were appropriately adjusted and refined with PHENIX[100]. Because of the relative flexibility of the C-terminal domain (AasS_C) in most AasS structures, they were built on the basis of the stable AasS_C configuration arising from AasS-bound AMP-PNP. The statistics on cryo-EM data collection and refinement are listed in Table 1 and all related structures were generated using UCSF Chimera and PyMol.

Statistics and reproducibility

All genetic and enzymatic experiments were performed at least three times. In addition to gel filtration, the AasS samples of cryo-EM were prepared in three replicates. In addition to a representative graph (for example, bacterial viability, western blot and urea gel) that was given as appropriate, the other data (for example, growth curves and ITC stoichiometry) were presented as the mean values ± s.d. from three independent experiments. The f(*x*) formula used to measure the s.d. value was implemented through STDEV.S in Microsoft Excel.

Reporting summary

Further information on research design is available in the Nature Portfolio Reporting Summary linked to this article.

Data availability

The refined coordinates and maps of the nine AasS structures in this study were deposited in the PDB and EM Data Bank with the following accession codes: PDB 8HZX and EMD-35091 for native AasS, PDB 8I3I and EMD-35153 for AasS bound by AMP-PNP, PDB 8I49 and EMD-35165 for the AasS–ATP complex, PDB 8I22 and EMD-35129 for E-pim-bound AasS, PDB 8I35 and EMD-35144 for C18:1-liganded AasS, PDB 8I51 and EMD-35190 for AasS complexed with M-pim-AMP, PDB 8I6M and EMD-35200 for AasS occupied by M-pim-AMP, PDB 8I8D and EMD-35248 for AasS–AMP-C18:1 and PDB 8I8E and EMD-35249 for the AasS–M-pim-ACP complex. All data needed to evaluate the conclusions in this paper are present in the paper and/or Supplementary Information. All *E. coli* strains expressing recombinant AasS and/or its mutants can be provided by Zhejiang University pending scientific review and a completed material transfer agreement. Requests for strains and plasmids should be submitted to Y.F. (fengyj@zju.edu.cn). Source data are provided with this paper.

References

83. Lin, S. & Cronan, J. E. The BioC *O*-methyltransferase catalyzes methyl esterification of malonyl-acyl carrier protein, an essential step in biotin synthesis. *J. Biol. Chem.* **287**, 37010–37020 (2012).
84. Liu, L. et al. Chasing the landscape for intrahospital transmission and evolution of hypervirulent carbapenem-resistant *Klebsiella pneumoniae*. *Sci. Bull.* **68**, 3027–3047 (2023).
85. Li, P. et al. Convergence of carbapenem resistance and hypervirulence in a highly-transmissible ST11 clone of *K. pneumoniae*: an epidemiological, genomic and functional study. *Virulence* **12**, 377–388 (2021).
86. Zhang, S. et al. Biochemical and structural characterization of the BioZ enzyme engaged in bacterial biotin synthesis pathway. *Nat. Commun.* **12**, 2056 (2021).
87. Flugel, R. S., Hwangbo, Y., Lambalot, R. H., Cronan, J. E. & Walsh, C. T. Holo-(acyl carrier protein) synthase and phosphopantetheinyl transfer in *Escherichia coli*. *J. Biol. Chem.* **275**, 959–968 (2000).
88. Shi, Y. et al. The opportunistic pathogen *Pseudomonas aeruginosa* exploits bacterial biotin synthesis pathway to benefit its infectivity. *PLoS Pathog.* **19**, e1011110 (2023).
89. Xu, Y. et al. Three enigmatic BioH isoenzymes are programmed in the early stage of mycobacterial biotin synthesis, an attractive anti-TB drug target. *PLoS Pathog.* **18**, e1010615 (2022).
90. Tang, Q. et al. *Mycobacterium smegmatis* BioQ defines a new regulatory network for biotin metabolism. *Mol. Microbiol.* **94**, 1006–1023 (2014).
91. Gabrielson, J. P., Randolph, T. W., Kendrick, B. S. & Stoner, M. R. Sedimentation velocity analytical ultracentrifugation and SEDFIT/c(s): limits of quantitation for a monoclonal antibody system. *Anal. Biochem.* **361**, 24–30 (2007).
92. Hu, Z. & Cronan, J. E. The primary step of biotin synthesis in mycobacteria. *Proc. Natl Acad. Sci. USA* **117**, 23794–23801 (2020).
93. Wei, W. et al. Molecular basis of BioJ, a unique gatekeeper in bacterial biotin synthesis. *iScience* **19**, 796–808 (2019).
94. Gao, R. et al. Structural and functional characterization of the FadR regulatory protein from *Vibrio alginolyticus*. *Front. Cell. Infect. Microbiol.* **7**, 513 (2017).
95. Mastronarde, D. N. Automated electron microscope tomography using robust prediction of specimen movements. *J. Struct. Biol.* **152**, 36–51 (2005).
96. Thompson, R. F., Iadanza, M. G., Hesketh, E. L., Rawson, S. & Ranson, N. A. Collection, pre-processing and on-the-fly analysis of data for high-resolution, single-particle cryo-electron microscopy. *Nat. Protoc.* **14**, 100–118 (2019).
97. Zheng, S. Q. et al. MotionCor2: anisotropic correction of beam-induced motion for improved cryo-electron microscopy. *Nat. Methods* **14**, 331–332 (2017).
98. Zhang, K. Gctf: real-time CTF determination and correction. *J. Struct. Biol.* **193**, 1–12 (2016).
99. Punjani, A., Rubinstein, J. L., Fleet, D. J. & Brubaker, M. A. cryoSPARC: algorithms for rapid unsupervised cryo-EM structure determination. *Nat. Methods* **14**, 290–296 (2017).
100. Adams, P. D. et al. PHENIX: a comprehensive Python-based system for macromolecular structure solution. *Acta Crystallogr. D* **66**, 213–221 (2010).
101. Emsley, P., Lohkamp, B., Scott, W. G. & Cowtan, K. Features and development of Coot. *Acta Crystallogr. D* **66**, 486–501 (2010).
102. Pettersen, E. F. et al. UCSF chimera—a visualization system for exploratory research and analysis. *J. Comput. Chem.* **25**, 1605–1612 (2004).

Acknowledgements
This work was supported by the National Science Fund for Distinguished Young Scholars (32125003, to Y.F.), the National Natural Science Foundation of China (32141001 and 31830001, to Y.F.; 32371250, to C.Z.), the National Key Research and Development Program of China (2022YFC2303900 and 2022YFC3704700, to Y.X.) and the Natural Science Foundation of Shanxi Province (2023-JC-YB-159, to T.C.). We thank L. Wu (Center of Cryo-EM, Zhejiang University) for technical assistance with AasS Cryo-EM data collection. We are also grateful to Y. Xu (Analysis Center for Agrobiology and Environmental Sciences, Zhejiang University) for technical assistance with LC–MS/MS and matrix-assisted laser desorption/ionization time-of-flight MS.

Author contributions
Y.F., C.Z. and X.Z. designed the research. Y.F., H.H., C.W., T.C., S.C., X.Z., Y.X., H.Z., M.H. and C.Z. conducted the research and analyzed the data. Y.F., C.Z., T.C., H.H., C.W., H.Z. and X.Z. wrote the paper.

Competing interests
The authors declare no competing interests.

Additional information
Extended data is available for this paper at https://doi.org/10.1038/s41594-024-01464-7.

Supplementary information The online version contains supplementary material available at https://doi.org/10.1038/s41594-024-01464-7.

Correspondence and requests for materials should be addressed to Chun Zhou, Xing Zhang or Youjun Feng.

Peer review information *Nature Structural & Molecular Biology* thanks Sujata Sharma and the other, anonymous, reviewer(s) for their contribution to the peer review of this work. Peer reviewer reports are available. Primary Handling Editor: Katarzyna Ciazynska, in collaboration with the *Nature Structural & Molecular Biology* team.

Reprints and permissions information is available at www.nature.com/reprints.

https://doi.org/10.1038/s41594-024-01464-7

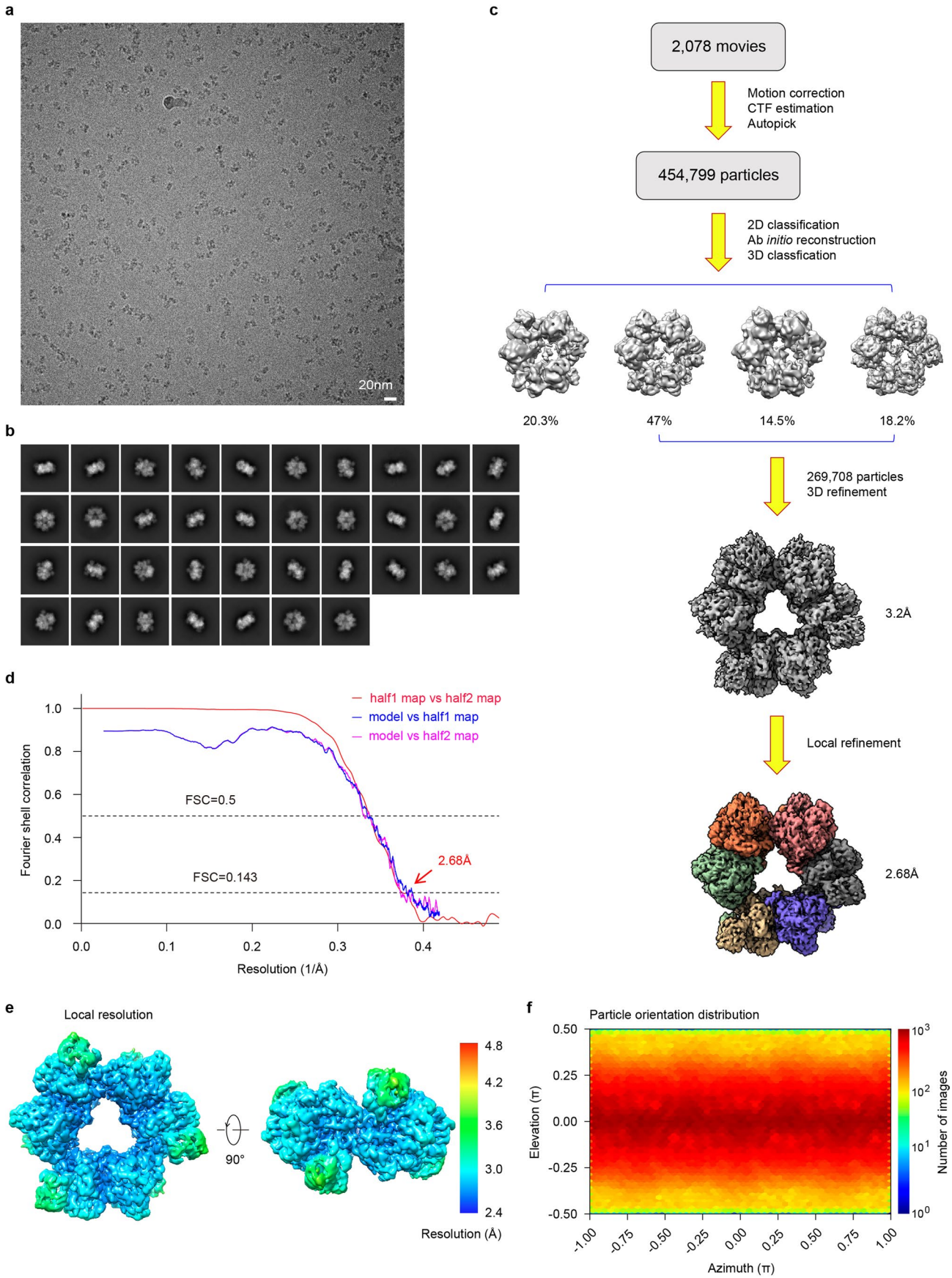

Extended Data Fig. 1 | Image-processing flowchart for AasS enzyme. a. Typical cryo-EM microscope images of AasS protein. **b.** Selected two-dimensional class averages of cryo-EM images of AasS particle. **c.** Scheme of three-dimensional classification, refinement and local refinement of cryo-EM particle images and the final 3D reconstitution of AasS at 2.68 Å. **d.** Gold-standard FSC curves of the final cryo-EM maps of AasS. **e.** Local resolution of apo-AasS in hexamer. **f.** Particle orientation distribution of apo AasS enzyme. Abbreviations: cryo-EM, Cryogenic electron microscopy.

https://doi.org/10.1038/s41594-024-01464-7

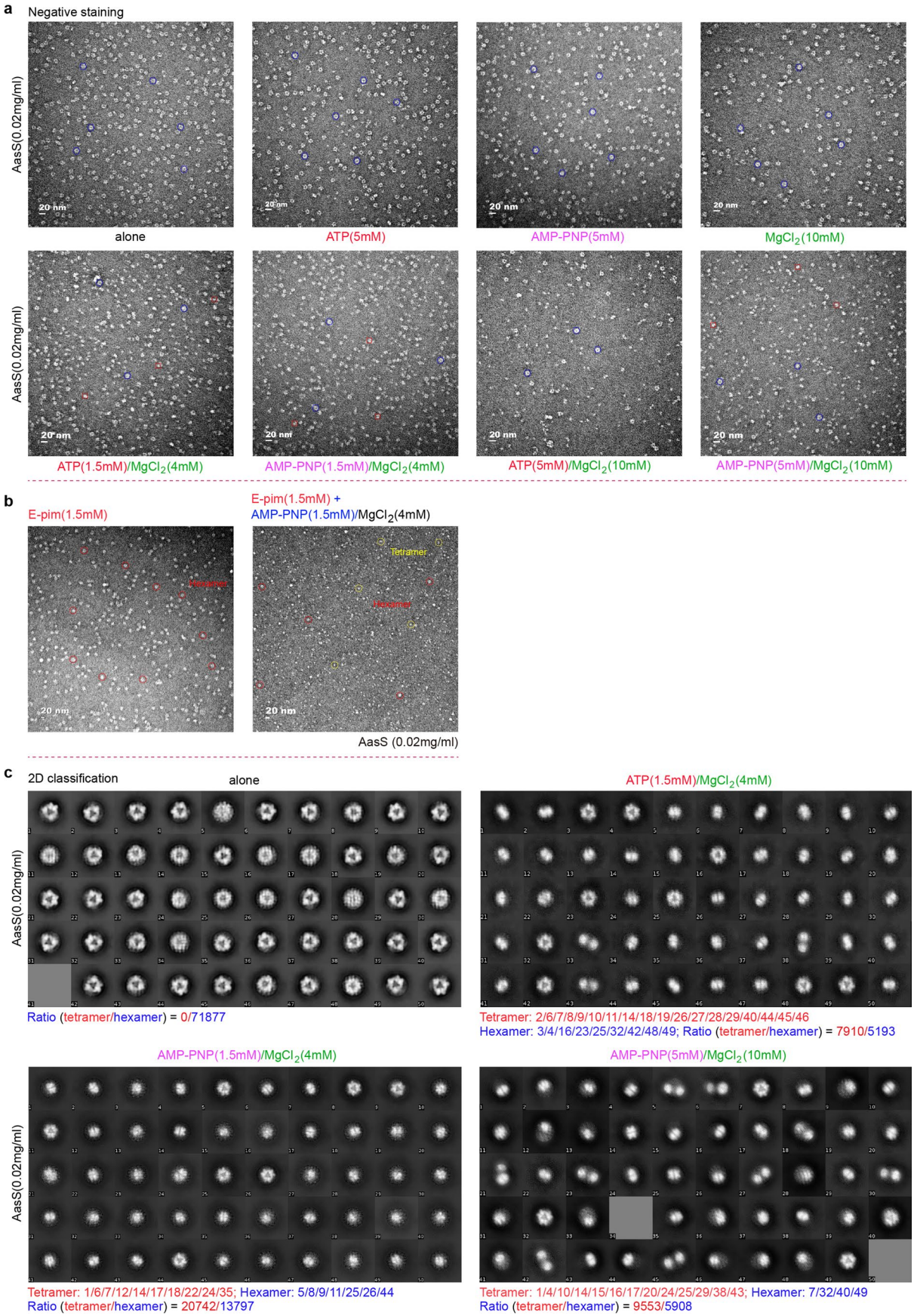

Extended Data Fig. 2 | See next page for caption.

https://doi.org/10.1038/s41594-024-01464-7

Extended Data Fig. 2 | Negative-staining analyses and 2D classification of AasS enzyme in diverse forms. a. Negative-staining analyses of AasS alone and its 7 kinds of complexes. As for the preparation of the negative-staining samples, AasS (0.02 mg/ml) protein was used. The seven AasS complexes are composed of three binary complexes that contains (i) ATP (5 mM), (ii) AMP-PNP (5 mM) & (iii) $MgCl_2$ (10 mM)], and four tertiary complexes including (i) ATP (1.5 mM)/$MgCl_2$ (4 mM), (ii) AMP-PNP (1.5 mM)/$MgCl_2$ (4 mM), (iii) ATP (5 mM)/$MgCl_2$ (10 mM) & (iv) AMP-PNP (5 mM)/$MgCl_2$ (10 mM). The AasS hexamer is indicated with a blue hexagon, and its tetramer is showed with a red square. The presence of $MgCl_2$ and ATP (and/or its analogue AMP-PNP) renders AasS enzyme to form tetramer as an intermediate state, along with its stable state of hexamer. **b**. Negative stain comparison suggested that AMP-PNP, a nonhydrolyzable ATP surrogate triggers conversion of AasS tetramer from its hexamer regardless of E-pimelic acid. As shown in negative staining (Panel Left), AasS appears as hexamer (indicated with a blue square) in the presence of E-pimelic acid. Notably, negative stain analysis unveiled that AMP-PNP enables the conversion of AasS from hexamer to tetramer (highlighted with a yellow square, Panel Right) even when E-pimelic acid is present. **c**. Contrasting 2D classification of the apo-AasS with its ATP/AMP-PNP (and/or $MgCl_2$)-liganded forms. 2D classification allowed the detection of 71,877 hexamer particles in the sample of AasS alone. By contrast, the co-occurrence of ATP (and/or AMP-PNP) and $MgCl_2$ enables that AasS tetrameric form, the presumable intermediate, largely accumulates accompanying the stable hexamer. Namely, the ratio of AasS particles (tetramer: hexamer) denotes (i) 7910: 5193 [ATP (1.5 mM)/$MgCl_2$ (4 mM)], (ii) 20742: 13797 [AMP-PNP (1.5 mM)/$MgCl_2$ (4 mM)], and (iii) 9553: 5908 [AMP-PNP (5 mM)/$MgCl_2$ (10 mM)].

https://doi.org/10.1038/s41594-024-01464-7

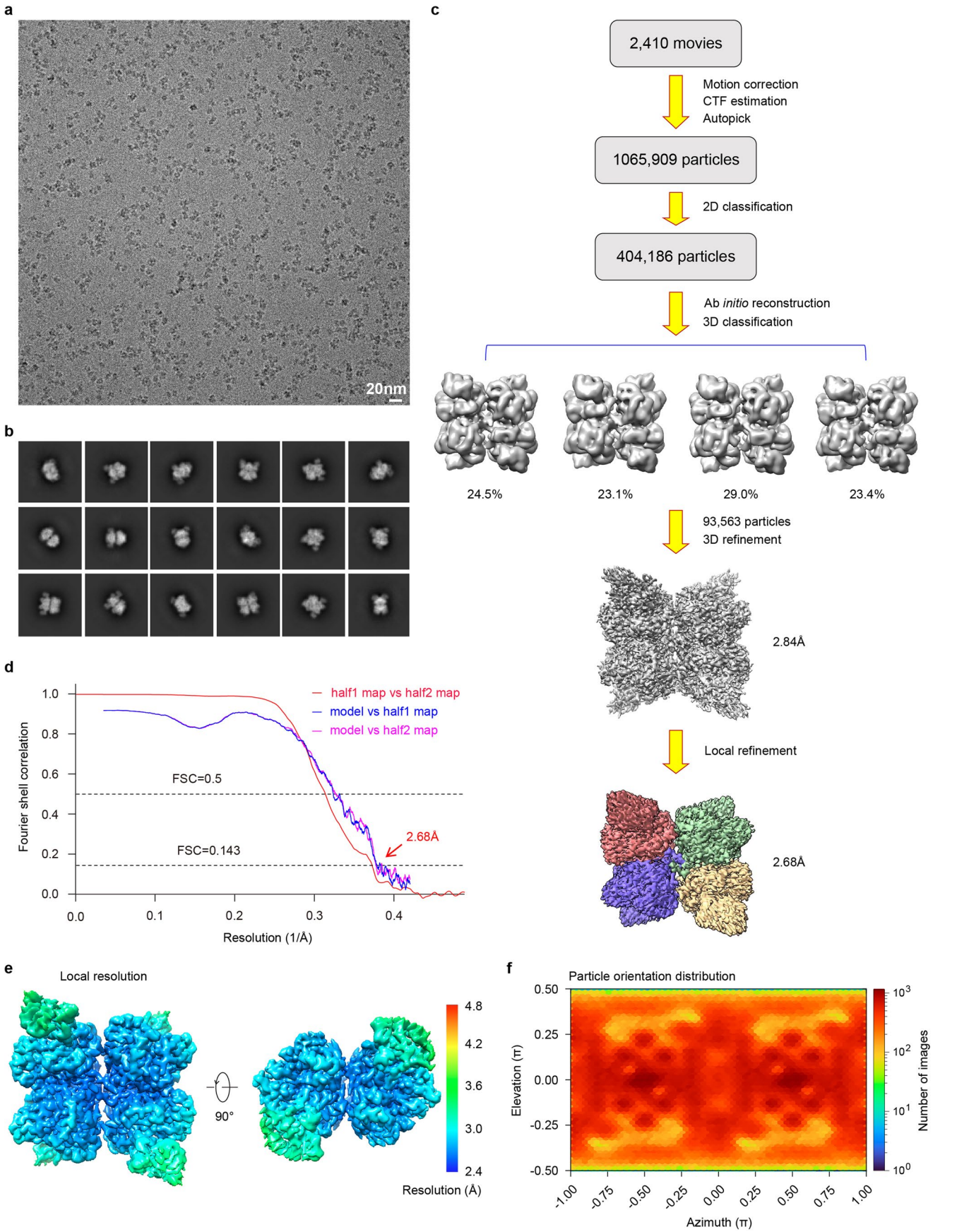

Extended Data Fig. 3 | See next page for caption.

https://doi.org/10.1038/s41594-024-01464-7

Extended Data Fig. 3 | Image-processing flowchart for AasS enzyme liganded with the ATP analogue, AMP-PNP. a. Representatives for cryo-EM microscope images of AasS complexed with AMP-PNP. **b**. Selected two-dimensional class averages of cryo-EM images of AasS/AMP-PNP complex particle. **c**. Scheme of three-dimensional classification, refinement and local refinement of cryo-EM particle images and the final 3D reconstitution of AasS/AMP-PNP complex at 2.68 Å. **d**. The FSC curve of the final cryo-EM maps of AasS/AMP-PNP. **e**. Local resolution of the tetrameric AasS liganded with AMP-PNP. **f**. Particle orientation distribution of AasS liganded with the analog AMP-PNP. Notably, slight density distortion has been observed for the outer regions of C-terminal domain due to the misalignment stemming from the flexibility of the C-terminal domain. The density for most of the tetramer and the AMP-PNP-Mg^{2+} is quite clear as shown in Supplementary Figs. 12, 14b and 15b.

https://doi.org/10.1038/s41594-024-01464-7

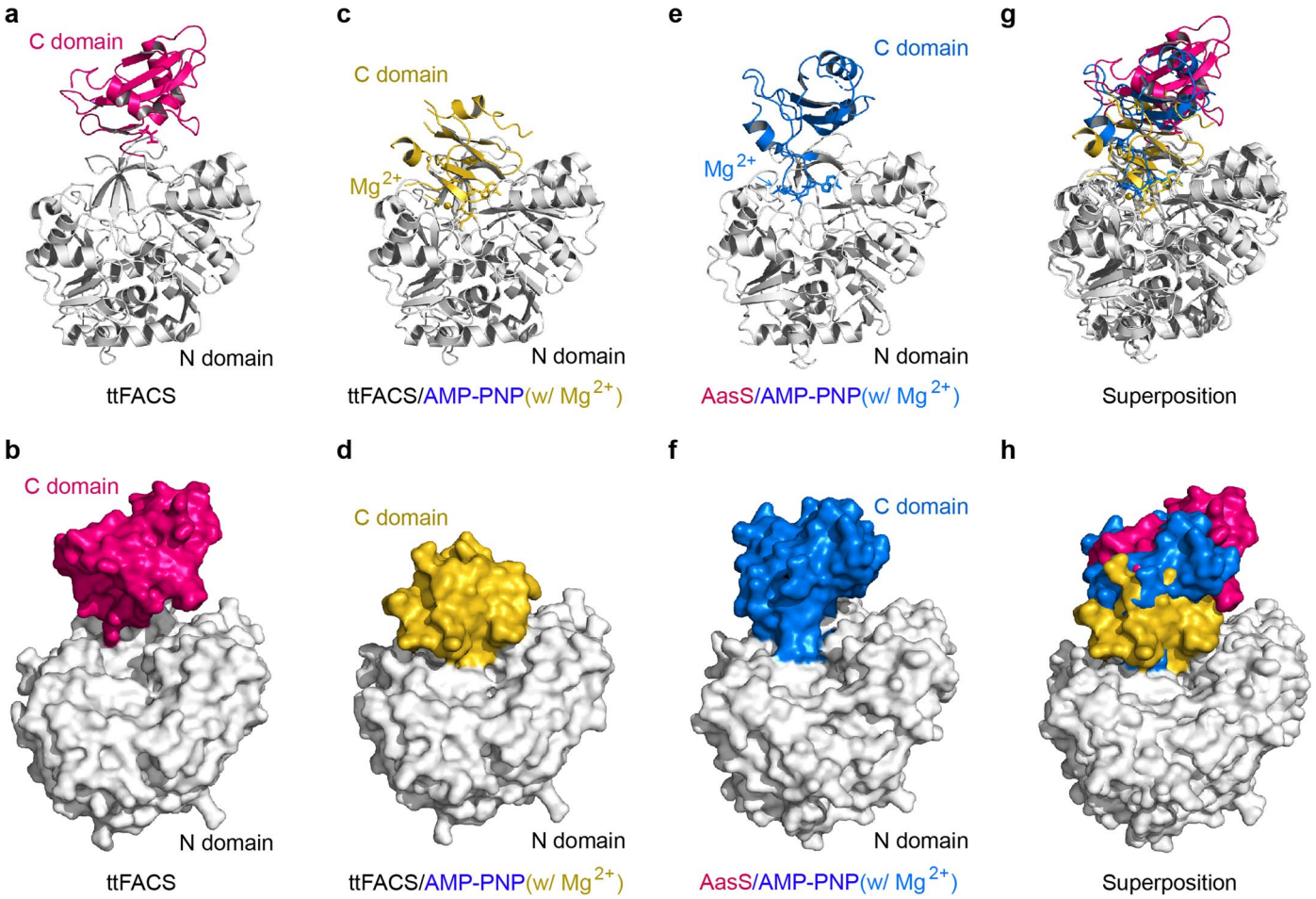

Extended Data Fig. 4 | Structural comparison of AasS and ttFACS in different conformations. Ribbon representation (**a**) and surface structure (**b**) of the monomeric form of apo-ttFACS. Ribbon structure (**c**) and surface illustration (**d**) for AMP-PNP-liganded ttFACS. The apo-ttFACS structure suggested that the C-terminal domain (colored hot-pink, in panels **a** & **b**) appears in open conformation. By contrast, it displays closed conformation (colored golden, in panels **c** & **d**), upon its binding to AMP-PNP, an ATP analogue. Ribbon diagram (**e**) and surface structure (**f**) of AasS/AMP-PNP complex. Unlike the scenarios seen with ttFACS/AMP-PNP complex, the C-terminal domain of AasS remains in open conformation (colored marine blue), albeit /despite of the AMP-PNP. The presence of Mg^{2+} ion is denoted with the symbol of 'w/ Mg^{2+}' (panels **c-f**). **g-h.** Structural superposition of apo-ttFACS, ttFACS/AMP-PNP, and AasS/AMP-PNP. The N-terminal domains from the two ttFACS conformations and AasS/AMP-PNP complex are colored white.

https://doi.org/10.1038/s41594-024-01464-7

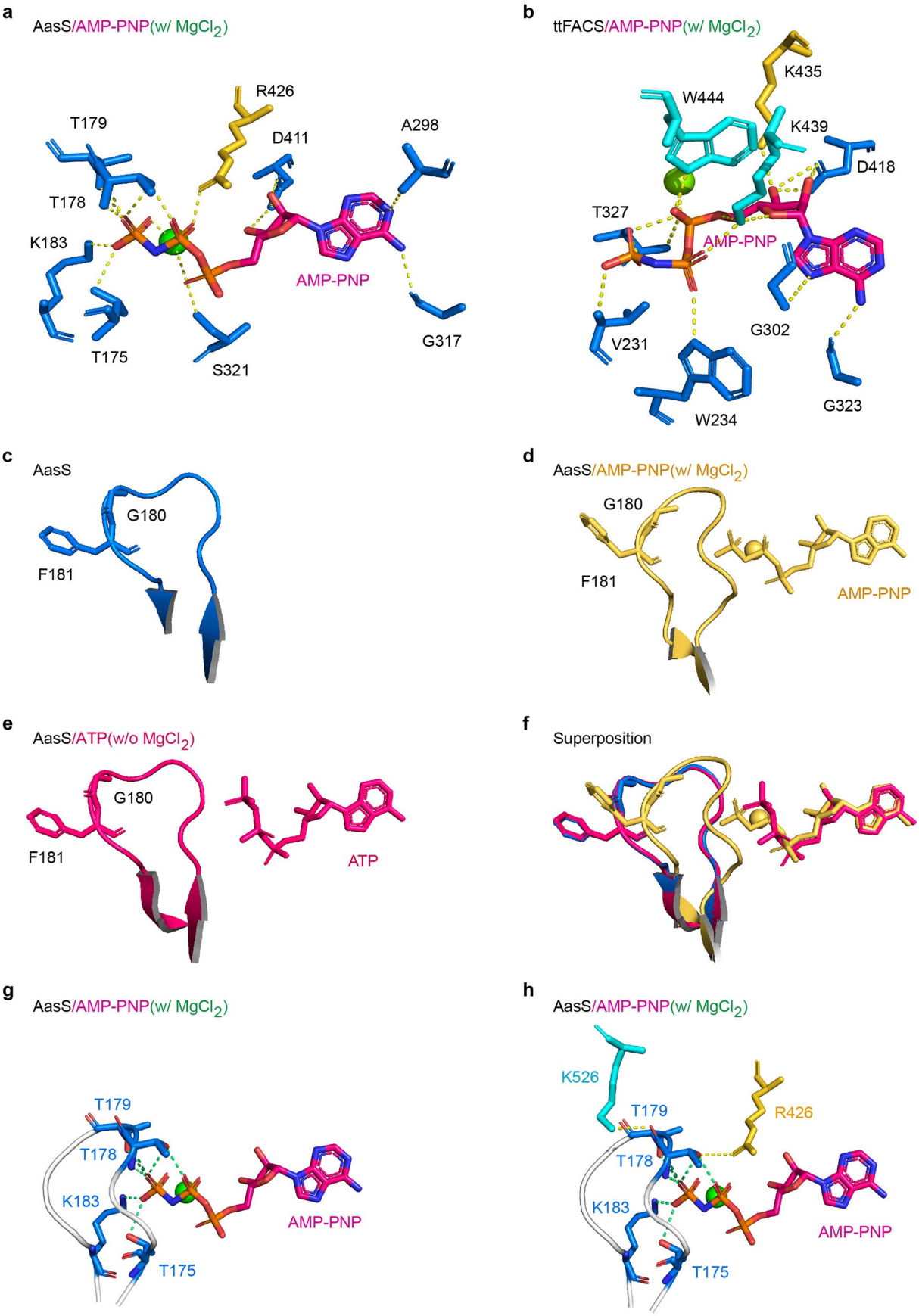

Extended Data Fig. 5 | See next page for caption.

https://doi.org/10.1038/s41594-024-01464-7

Extended Data Fig. 5 | Structural insight into the contacts of ATP/AMP-PNP with AasS and its comparison with ttFACS. Comparative analyses for polar contacts of the ATP analogue, AMP-PNP with AasS (**a**) and ttFACS (**b**). The residues of AasS (and/or ttFACS) surrounding AMP-PNP are shown with colorful sticks. As for AasS, the eight residues at N-terminus are colored marine blue (namely T175, T178, T179, K183, A298, G317, S321, and D411), and the only one (R426) located at L motif is labelled golden (in panel **a**). In the case of ttFACS, two C-terminal residues (K439 and W444, in cyan) are proposed, in addition to six ones at N-terminus (V231, W234, G302, G323, T327, and D418, in marine blue) and a single one on L loop (K435, in golden). AMP-PNP exhibits direct contact with the C-terminal domain of ttFACS (in panel **b**), whereas not in the case of AasS (in panel **a**). This direct interaction is presumed to benefit closing C-domain of ttFACS. **c**. Structural snapshot of Loop (174-184) in apo-AasS. Conformations of Loop (174-184) in AasS enzymes complexed with AMP-PNP (**d**) and M-pim-AMP (**e**). Two residues (G180 and F181, indicated with sticks) are believed to participate in the hydrophobic interaction on the trimer interface of AasS hexamer. **f**. Structural comparison of AasS with and without ligands suggested the conformational flexibility of Loop (174-184). Clearly, Loop (174-184) undergoes certain conformational transition/alternation upon AMP-PNP binding, and the altered conformation can be restored following the formation of M-pim-AMP from ATP and M-pimelate. **g**. A glimpse of Loop (174-184) having polar contacts with AMP-PNP via its four residues (T175, T178, T179, and K183). **h**. Polar contacts of T178 with R426 in L motif domain and near-end K526 at C-terminus. Conformational alteration of N-terminal Loop (174-184) of AasS is undergone upon AMP-PNP binding. As such, the AasS polymer forms, featuring with C-terminal domain closed. However, in the case of ttFACS, AMP-PNP directly binds to and thereby closes C-terminal domain. The presence of $MgCl_2$ is shown with 'w/ $MgCl_2$' (panels **a-b**, **d** & **g-h**).

https://doi.org/10.1038/s41594-024-01464-7

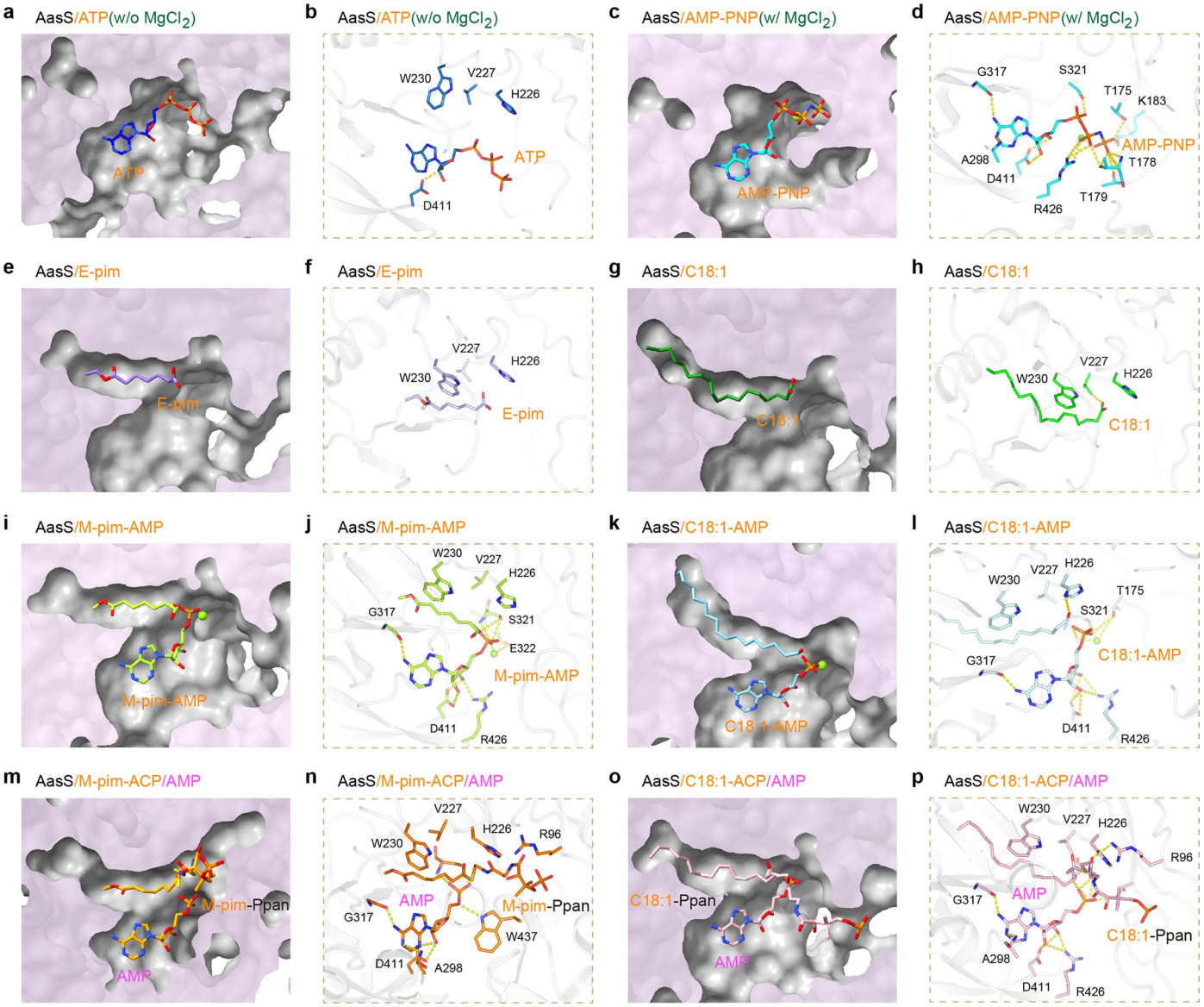

Extended Data Fig. 6 | Contrasting the bindings of AasS to diverse substrates/intermediates. a-b. ATP-binding cavity of AasS and its relevant /neighboring residues. **c-d.** The tunnel and residues of AasS occupied with AMP-PNP, a nonhydrolyzable ATP analogue The absence of $MgCl_2$ is given with 'w/o $MgCl_2$' (panels **a**-**b**), and its presence is shown with 'w/ $MgCl_2$' (panels **c**-**d**). **e-f.** Cut-away view of AasS binding E-pim substrate. **g-h.** Structural analyses of AasS interaction with E-C18:1 substrate. **i-j.** A structural glimpse of AasS occupied with M-pim-AMP intermediate. **k-l.** Structural snapshot for the occupancy of AasS by its C18:1-AMP intermediate. **m-n.** Structural insights in the ligand cavity of AasS with the two products M-pim-ACP and AMP. **o-p.** Structural presentation of the binding of AasS to its two products C18:1-ACP and AMP.

https://doi.org/10.1038/s41594-024-01464-7

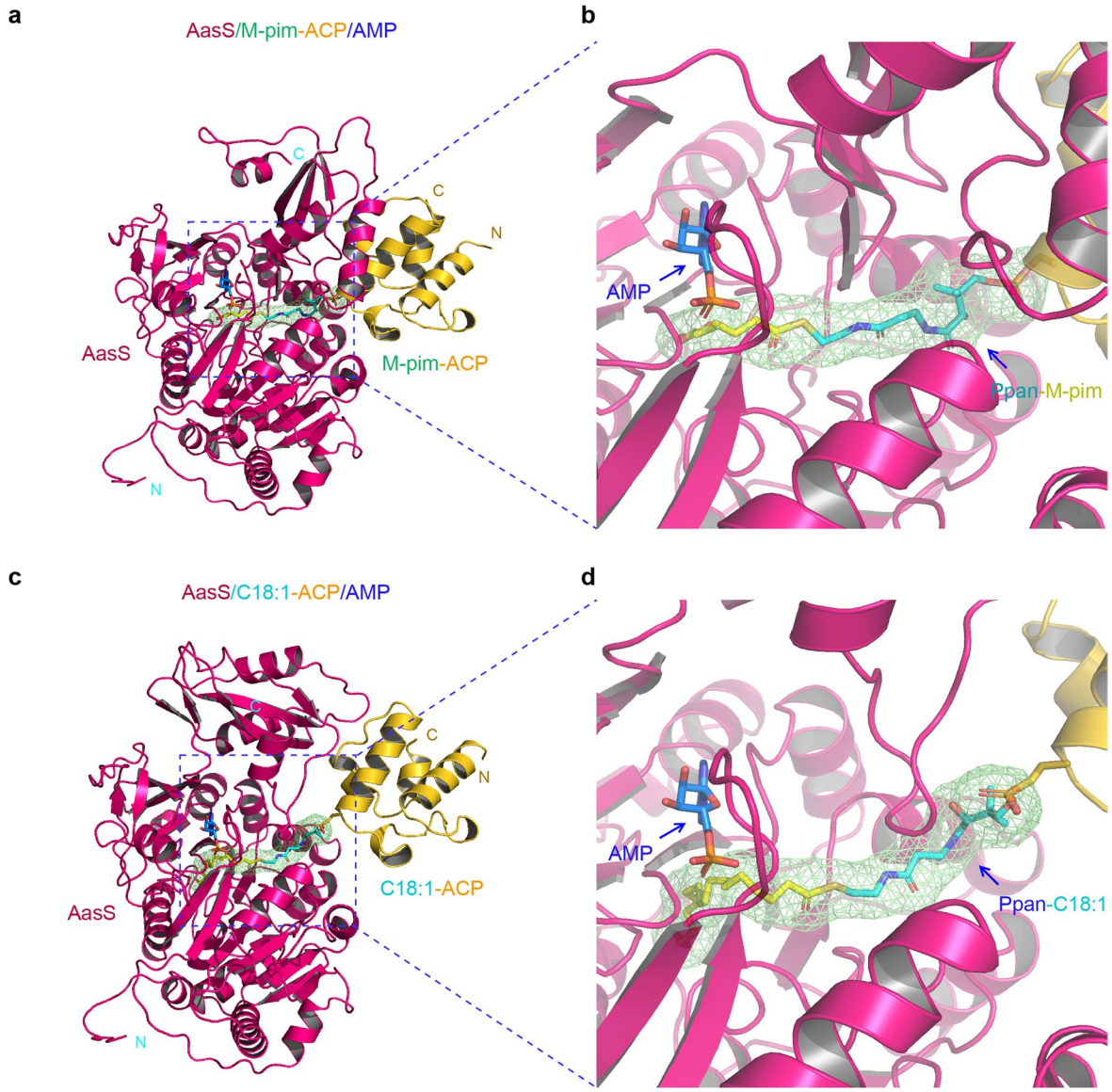

Extended Data Fig. 7 | Structural analysis of AasS complexed with two acyl-ACP products (M-pim-ACP and C18:1-ACP) in the presence of AMP. a. Ribbon representation of the AMP-bound AasS complexed with M-pim-ACP. **b**. An enlarged view of the bound AMP and Ppan-M-pim ligands. **c**. Ribbon structure of AasS/C18:1-ACP complex in the presence of AMP. **d**. Expanded view of the bound ligands of AMP and Ppan-C18:1. AasS is colored magenta, and ACP is colored gold. AMP and Ppan-M-pim are displayed as sticks, in which AMP is colored blue, Ppan is in teal and M-pim (or C18:1) is shown in yellow. The green mesh is the ligand electron density map, which is contoured at 0.427V/3.95rmsd for Ppan-M-pim (panel **b**), and 0.307V/2.80rmsd for Ppan-C18:1 (panel **d**). Designations: Ppan, Phosphopantetheine; Ppan-M-pim, Ppan-linked methyl pimelic acid; Ppan-C18:1, Ppan-tethered oleic acid.

https://doi.org/10.1038/s41594-024-01464-7

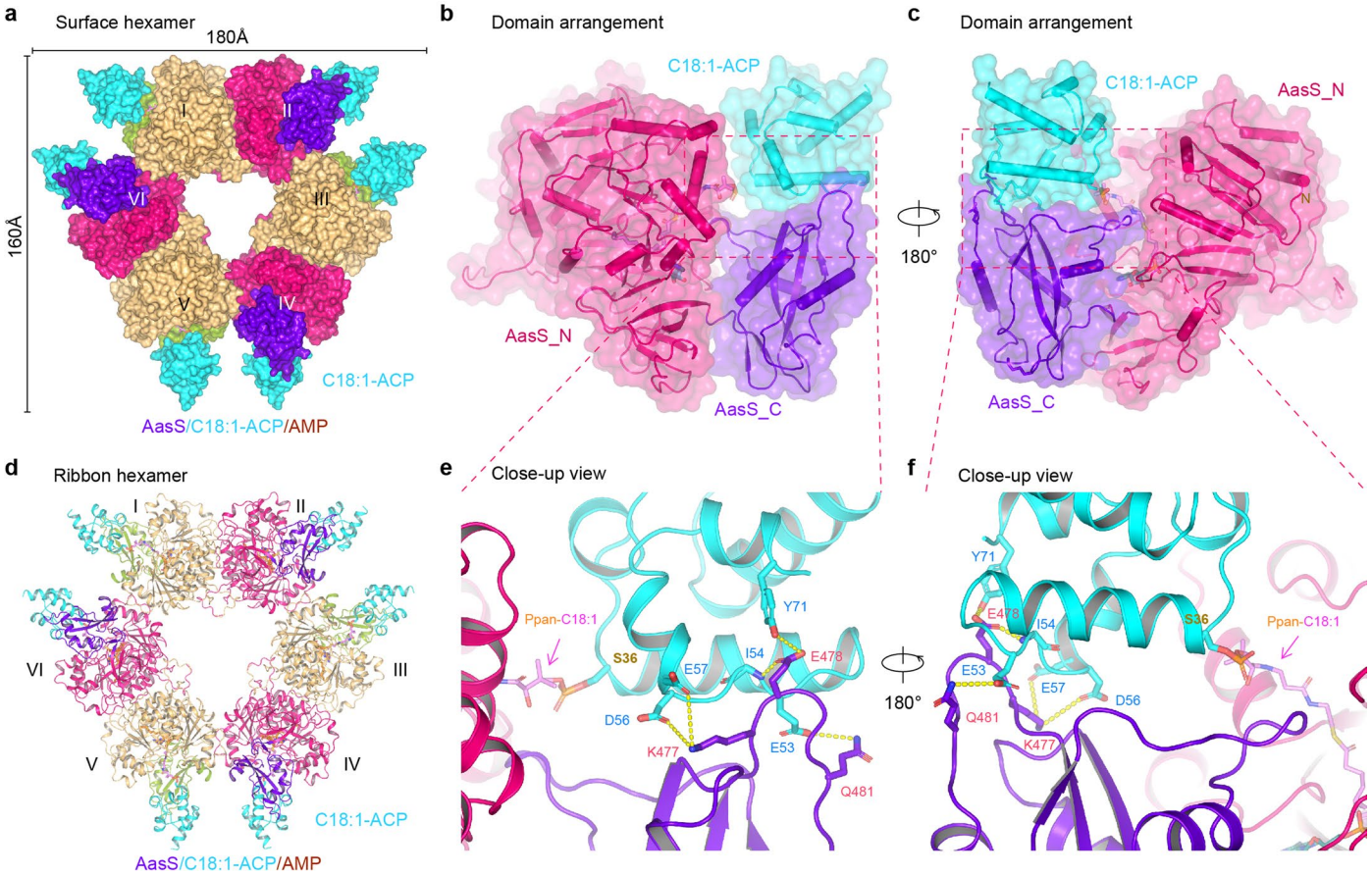

Extended Data Fig. 8 | Structural elucidation of C18:1-ACP binding interface on AasS. a. Surface representation of AasS/C18:1-ACP hexamer. **b-c**. Domain arrangement of each AasS/C18:1-ACP complex. AasS_N domains are colored in beige and hot-pink, AasS_C domains are colored in light-green and purple, and C18:1-ACP molecules are colored cyan. **d**. Ribbon representation of AasS/C18:1-ACP hexamer. **e-f**. Close-up view of AasS/C18:1-ACP interface that is mostly composed of electrostatic interaction and/or hydrogen bond network. Here, α-helices are displayed as cylinders.

https://doi.org/10.1038/s41594-024-01464-7

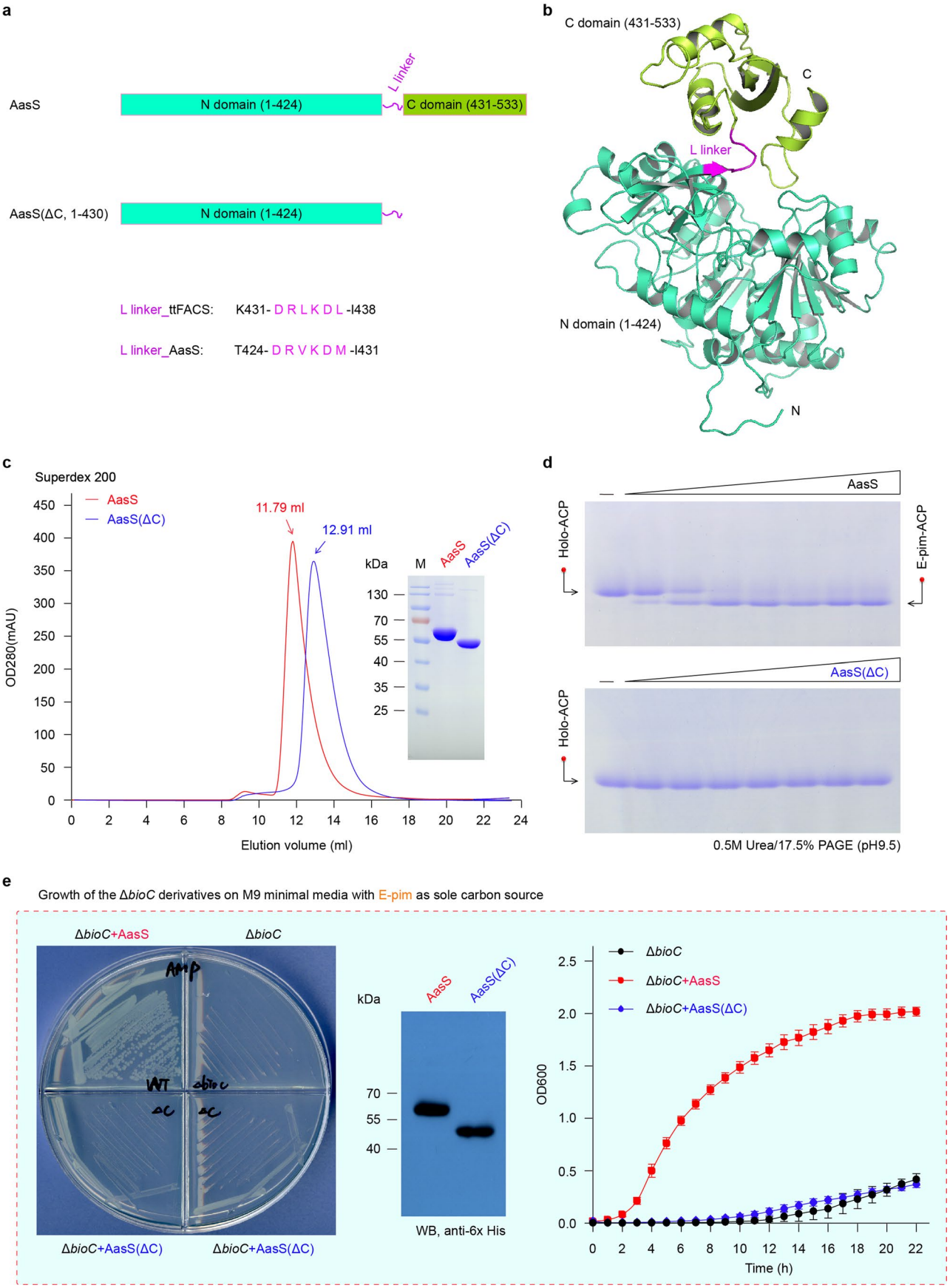

Extended Data Fig. 9 | See next page for caption.

https://doi.org/10.1038/s41594-024-01464-7

Extended Data Fig. 9 | The importance of C-domain in AasS action. a. Linear diagram for AasS and its deletion mutant, AasS(ΔC, 1-430). AasS is composed of a N-terminal domain (1-424 aa) and a C-terminal domain (431-533 aa), and the two domains are connected by L linker, a short 6-residue loop (425-430 aa). AasS(ΔC, 1-430), thereafter called AasS(ΔC), refers to the deletion mutant of AasS that retains the N-domain and its adjacent linker, but lacks a full C-terminal domain(431-533 aa). The sequences of L linker separately denote '$D^{425}R^{426}V^{427}K^{428}D^{429}M^{430}$' for AasS, and '$D^{432}R^{433}L^{434}K^{435}D^{436}L^{437}$' for ttFACS. **b**. Ribbon presentation of AasS structure highlighting the two separated domains. The N-domain is colored yellow, the C-domain is indicated with green, and L linker is shown in magenta. **c**. Use of gel filtration to analyze the truncated version of AasS, AasS(ΔC). A Superdex 200 increase column was applied to carry out size exclusion chromatography, and the inset gel of SDS-PAGE (12%) verified identity and purity of the resultant AasS and its derivative. **d**. Unlike the wild-type AasS, the AasS(ΔC) mutant lose the *in vitro* activity of ligating of holo-ACP species with mono-ethyl pimelate. Conformationally-sensitive native gel [0.5 M Urea/17.5% PAGE(pH 9.5)] was applied to differentiate the E-pim-ACP product synthesized by AasS from its reactant of holo-ACP. The symbol of minus '−' on the top of native gel denotes no addition of AasS [or AasS(ΔC)] enzyme, whereas the triangle on the right hand refers to varied enzymatic level ranging from 1.5, 3.0, 6.0, 15.0, 30.0, to 60.0 nM. **e**. The removal of C-domain from AasS impairs its ability to allow growth of the Δ*bioC* biotin auxotrophic strain of *E. coli* on the non-permissive condition of minimal medium M9 with mono-ethyl pimelate as the sole carbon source. Apart from growth curves, the occurrence of the Δ*bioC* biotin auxotroph on M9 agar plates was determined as described in Fig. 4. Prior to the functional analyses, Western blot was conducted to verify expression of the truncated mutant, AasS(ΔC) in the Δ*bio*C recipient strain (inside gel). Designations: N, N terminus; C, C terminus; ml, milli-liter; ACP, acyl carrier protein; E-pim-ACP, mono-ethyl pimeloyl ACP; OD600, optical density at the wave length of 600 nm.

https://doi.org/10.1038/s41594-024-01464-7

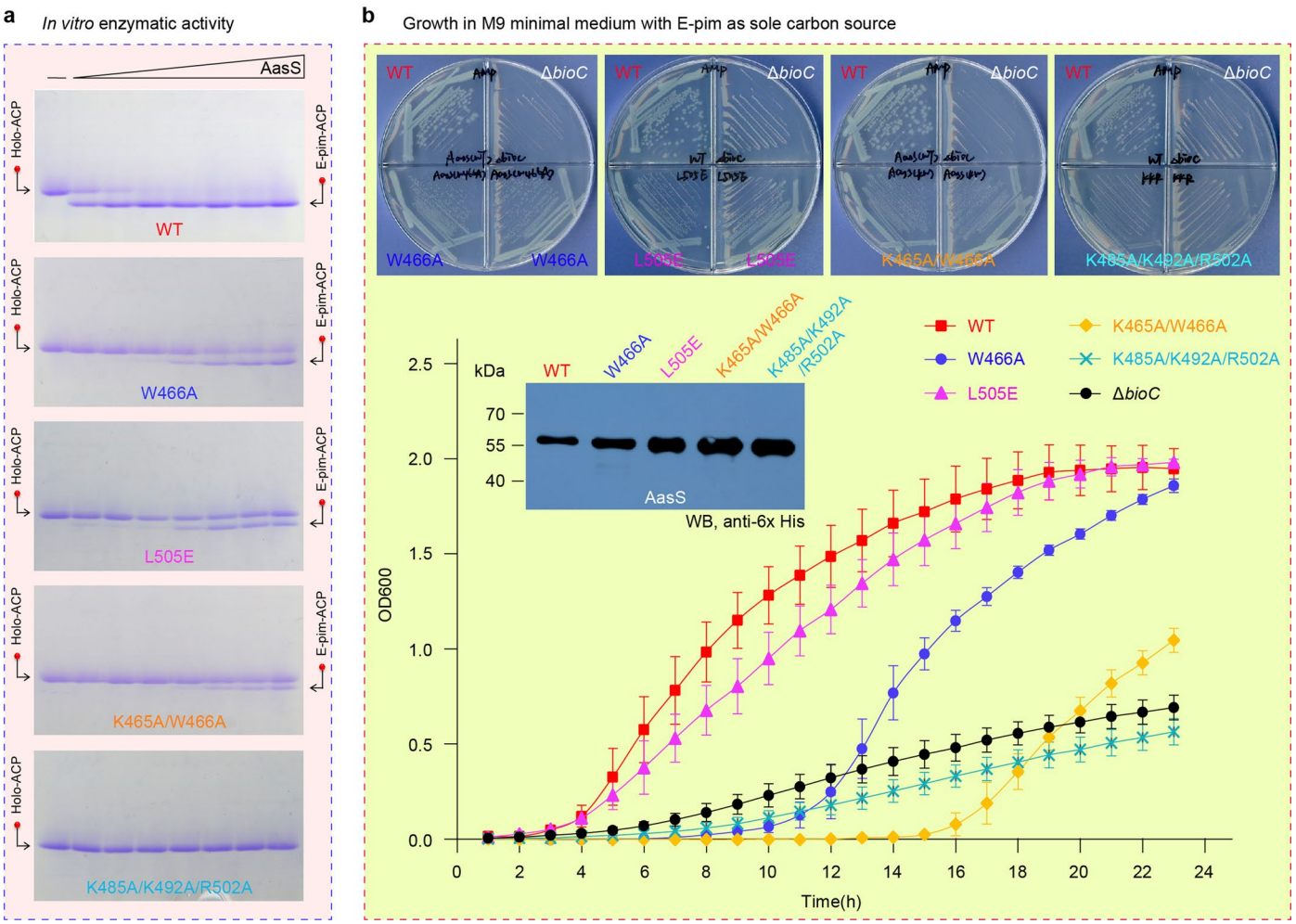

Extended Data Fig. 10 | Structure-guided functional analyses of the ACP-binding interface on the AasS enzyme. a. The *in vitro* enzymatic assays for AasS/M-pim-ACP interface. Four mutants of AasS protein were prepared and tested here, including two single mutants (W466A and L505E), and a double mutant (K465A/W466A), a triple mutant (K485A/K492A/R502A). **b**. The maintenance of AasS/M-pim-ACP interface is critical for AasS activity *in vivo*. Apart from growth curves, bacterial viability of the Δ*bioC* biotin auxotroph on M9 agar plates was determined as described in Fig. 5. Four mutants were subjected to Western blot analysis prior to the functional determination. In comparison to L505E having a minor role, W466A and K465A/W466A impairs greatly AasS activity. The loss of function is assigned to the triple mutant of AasS(K485A/K492A/R502A).

nature portfolio

Corresponding author(s): Youjun Feng

Last updated by author(s): May 7, 2024

Reporting Summary

Nature Portfolio wishes to improve the reproducibility of the work that we publish. This form provides structure for consistency and transparency in reporting. For further information on Nature Portfolio policies, see our Editorial Policies and the Editorial Policy Checklist.

Statistics

For all statistical analyses, confirm that the following items are present in the figure legend, table legend, main text, or Methods section.

n/a	Confirmed
☐	☒ The exact sample size (*n*) for each experimental group/condition, given as a discrete number and unit of measurement
☐	☒ A statement on whether measurements were taken from distinct samples or whether the same sample was measured repeatedly
☒	☐ The statistical test(s) used AND whether they are one- or two-sided *Only common tests should be described solely by name; describe more complex techniques in the Methods section.*
☒	☐ A description of all covariates tested
☒	☐ A description of any assumptions or corrections, such as tests of normality and adjustment for multiple comparisons
☐	☒ A full description of the statistical parameters including central tendency (e.g. means) or other basic estimates (e.g. regression coefficient) AND variation (e.g. standard deviation) or associated estimates of uncertainty (e.g. confidence intervals)
☒	☐ For null hypothesis testing, the test statistic (e.g. *F*, *t*, *r*) with confidence intervals, effect sizes, degrees of freedom and *P* value noted *Give P values as exact values whenever suitable.*
☒	☐ For Bayesian analysis, information on the choice of priors and Markov chain Monte Carlo settings
☒	☐ For hierarchical and complex designs, identification of the appropriate level for tests and full reporting of outcomes
☒	☐ Estimates of effect sizes (e.g. Cohen's *d*, Pearson's *r*), indicating how they were calculated

Our web collection on statistics for biologists contains articles on many of the points above.

Software and code

Policy information about availability of computer code

Data collection	UNICORN 7.0 (Version 7.0.0.953), SPECTROtar Nano (Version 5.50), MicroCal PEAQ-ITC Control software (Version 1.21), Serial EM (Version 3.8), EPU (Version 3.6.0.6389)
Data analysis	Image J (Version 1.53k), Microsoft 365 (Version 18.2311.1071.0), MicroCal PEAQ-ITC Analysis Software (Version 1.0.0.1259), SEDfit (Version 15.01b of 2015), Proteome Discoverer (Version 2.0), cisTEM (Version 1.0.0), CryoSPARC (Version 4.3.1), WinCoot (Version 0.9.8.1) CCP4, UCSF Chimera X (Version 1.3), Chimera (Version 1.16), Phenix (Version 1.20.1-4487), PyMOL (Version 2.6.0a0)

For manuscripts utilizing custom algorithms or software that are central to the research but not yet described in published literature, software must be made available to editors and reviewers. We strongly encourage code deposition in a community repository (e.g. GitHub). See the Nature Portfolio guidelines for submitting code & software for further information.

Data

Policy information about availability of data

All manuscripts must include a data availability statement. This statement should provide the following information, where applicable:

- Accession codes, unique identifiers, or web links for publicly available datasets
- A description of any restrictions on data availability
- For clinical datasets or third party data, please ensure that the statement adheres to our policy

The refined coordinates and maps of the AasS structures in this study have been deposited in the Protein data bank (PDB) and Electron Microscopy Data Bank

(EMD) with the following access codes: (i) PDB:8HZX and EMD-35091 for native AasS; (ii) PDB: 8I3I and EMD- 35153 for AasS bound by AMP-PNP; (iii) PDB: 8I49 and EMD- 35165, for AasS/ATP complex; (iv) PDB: 8I22 and EMD-35129 for E-pim-bound AasS; (v) PDB: 8I35 and EMD-35144 for C18:1-liganded AasS; (vi) PDB: 8I51 and EMD-35190 for AasS complexed with M-pim-AMP; (vii) PDB: 8I6M and EMD-35200 for AasS occupied with M-pim-AMP; (viii) PDB: 8I8D and EMD-35248 for AasS/AMP-C18:1; and (ix) PDB: 8I8E and EMD-35249 for AasS/M-pim-ACP complex. All data needed to evaluate the conclusions in this paper are present in the paper and/or the Supplementary Materials. All other data and materials are available upon request from the corresponding author. Source data are provided with this paper.

Research involving human participants, their data, or biological material

Policy information about studies with human participants or human data. See also policy information about sex, gender (identity/presentation), and sexual orientation and race, ethnicity and racism.

Reporting on sex and gender	N/A
Reporting on race, ethnicity, or other socially relevant groupings	N/A
Population characteristics	N/A
Recruitment	N/A
Ethics oversight	N/A

Note that full information on the approval of the study protocol must also be provided in the manuscript.

Field-specific reporting

Please select the one below that is the best fit for your research. If you are not sure, read the appropriate sections before making your selection.

☒ Life sciences ☐ Behavioural & social sciences ☐ Ecological, evolutionary & environmental sciences

For a reference copy of the document with all sections, see nature.com/documents/nr-reporting-summary-flat.pdf

Life sciences study design

All studies must disclose on these points even when the disclosure is negative.

Sample size	There was no predetermined sample size. Regarding Cryo-EM data collection, since the first set of data was collected with 2,078 movies and a particle count of 770,000 particles, which is a sufficient amount of data to obtain the map with a resolution of up to 2.8 Angstroms, subsequent data collections have been based on a minimum of 2,000 micrographs. Based on previous experience, all functional assay were performed with at least three independent replications.
Data exclusions	No data was excluded during the analysis.
Replication	All experiments have been reproduced for no less than three times.
Randomization	Randomization has no relevance in the study of Cryo-EM for structure analysis, bacterial functional assays and functional experiments of purified proteins.
Blinding	The experiments mentioned in this study need to follow a defined process as well as control variables without the use of blinding.

Reporting for specific materials, systems and methods

We require information from authors about some types of materials, experimental systems and methods used in many studies. Here, indicate whether each material, system or method listed is relevant to your study. If you are not sure if a list item applies to your research, read the appropriate section before selecting a response.

Materials & experimental systems

n/a	Involved in the study
☐	☒ Antibodies
☒	☐ Eukaryotic cell lines
☒	☐ Palaeontology and archaeology
☒	☐ Animals and other organisms
☒	☐ Clinical data
☒	☐ Dual use research of concern
☒	☐ Plants

Methods

n/a	Involved in the study
☒	☐ ChIP-seq
☒	☐ Flow cytometry
☒	☐ MRI-based neuroimaging

Antibodies

Antibodies used

1. Anti-His Tag Monoclonal Antibody [HIS.H8], 1:8000, EarthOx Life Sciences, cat # E022020-02
2. HRP AffiniPure Goat Anti-Mouse IgG(H+L), 1:5000, EarthOx Life Sciences, cat # E030110-02

Validation

1. Anti-His Tag Monoclonal Antibody [HIS.H8] (https://pmt58cea3-pic8.websiteonline.cn/upload/E022020_v3qp.pdf)
2. HRP AffiniPure Goat Anti-Mouse IgG(H+L) (https://pmt58cea3-pic8.websiteonline.cn/upload/E030110_dle2.pdf)

Plants

Seed stocks

Not applied

Novel plant genotypes

Not applied

Authentication

Not applied